Evidence of gravity wave contribution to vertical shear and mixing in the lower stratosphere

Madhuri Umbarkar[1], Daniel Kunkel[1], Annette Miltenberger[1], Hans-Christoph Lachnitt[1], Thorsten Kaluza[2], Cornelis Schwenk[1], and Peter Hoor[1]

[1]Institute for Atmospheric Physics, Johannes Gutenberg University Mainz, Germany
[2]Department of Meteorology, University of Reading, Reading, UK

Correspondence: Madhuri Umbarkar (mumbarka@uni-mainz.de)

Abstract. Evidence is presented which illustrates the role of atmospheric gravity wave (GW) induced shear as a mechanism for the occurrence of clear air turbulence and mixing of air masses with different chemical composition in the lower stratosphere. This study investigates the relation of GWs, vertical wind shear and turbulence as well as the potential consequence of this relation onto the trace species distribution in the lowermost stratosphere (LMS) over the North Atlantic. The analysis of airborne observations, reanalysis and forecast data highlight the impact of mesoscale dynamics in relation to GWs on the constituents around the tropopause. The GWs propagate through highly sheared flow above the jet stream maximum, perturbing background wind shear and static stability, and thereby creating conditions conducive to turbulent mixing in the LMS. The observed significant correlation between GW-induced momentum flux and enhanced shear perturbations confirms the role of GWs in driving potential turbulence and facilitating trace gas exchange. Further analysis of turbulence diagnostics including Richardson number on large-scale and turbulence indices (TI1, TI2) on small-scale suggests that GWs produce shear which leads to the occurrence of clear air turbulence.

1 Introduction

Atmospheric gravity waves (GW), ubiquitous buoyancy-driven oscillations, play a crucial role in a wide variety of atmospheric processes. These gravity waves can initiate and organize convection (Zhang et al., 2001), as well as generate and modulate atmospheric turbulence (Shapiro, 1980). Also, GWs redistribute momentum and energy through vertical propagation, which affects the general circulation, especially for exchange of air masses between troposphere and stratosphere (Holton et al., 1995).

Generally speaking, GWs can be generated and activated by topographic forcing, convection, shear instability, as well as geostrophic adjustment related to jets, fronts, and sources of strong diabatic heating (Hooke, 1986; Fritts and Alexander, 2003; Kim et al., 2003; Plougonven et al., 2008). Orographic GWs are generated through the interaction between atmospheric flow and surface topographic features, producing mainly vertically propagating waves that influence the energy and momentum balance in the UTLS (Durran, 1995; Lachnitt et al., 2023). These GWs propagate further upwards through the stratosphere where they dissipate and influence the atmospheric circulation, particularly the Brewer-Dobson circulation (Achatz et al., 2024, and reference therein). Convective sources generate GWs through latent heat release and rapid vertical motions as

in thunderstorms, often observed in both tropical and extratropical regions (Fritts and Alexander, 2003; Alexander et al., 2010). Moreover, Lane et al. (2001) and Lane and Sharman (2006) emphasized that convective clouds generate GWs when the convective updraft rapidly decelerates. The distribution of different GW sources largely controls the global distribution of GWs and their impact on atmospheric stability and transport processes.

In the extratropics, baroclinic waves represent an important, albeit less well understood source of GWs. Surface fronts and upper level jet streams associated with baroclinic wave development generate GWs, primarily through spontaneous imbalance, i.e., deviations from balanced flow trigger wave emission (Plougonven and Zhang, 2014; Zhang et al., 2015b). Regions of baroclinic instability, particularly along jet streaks and frontal zones, are hotspots for non-orographic GW activity. Moreover, tropospheric moist processes turn out to play an important role in the generation of GW from mid-latitude and high-latitude weather systems (e.g. Wei and Zhang, 2014; Plougonven et al., 2015; Holt et al., 2017). In such regions, interactions between divergent flow (or GWs) and the background flow (Trier et al., 2020) lead to shear generation and turbulence (e.g., O'sullivan and Dunkerton, 1995; Plougonven and Snyder, 2005; Zülicke and Peters, 2006; Kaluza et al., 2021). GWs excited from tropospheric weather systems (or synoptic eddies) can propagate into the UTLS and middle atmosphere. Upon dissipation, these waves deposit momentum and energy, leading to forcing of the background flow at upper levels and thereby contribute to large-scale dynamics such as the Brewer–Dobson circulation (Alexander et al., 2010; Achatz et al., 2024, and references therein). Their influence also extends to the tropopause structure and stratosphere–troposphere exchange processes, that relate the small-scale dynamics with planetary scale overturning circulation (Plougonven et al., 2008; Dörnbrack, 2024; Jovanovic, 2025). Despite their ubiquity, the mechanisms governing GW generation within baroclinic system remain poorly understood, necessitating further investigation to quantify their role in shaping the UTLS and beyond.

Orographic GWs, despite exhibiting significant seasonality and a high degree of transience, serve as hotspots for turbulence at the tropopause (Fritts and Alexander, 2003; Alexander and Grimsdell, 2013; Rapp et al., 2021). Lachnitt et al. (2023) have shown that GW induced turbulence can have a persistent effect on the distribution of species and hence potential forcing impact on radiatively active tracer species by changing their isentropic gradients (Dörnbrack et al., 2025). Consequently, the mixing induced by GWs contributes to the overall mixing-induced uncertainty of radiative forcing (Riese et al., 2012).

GWs likewise play a key role in shaping the thermodynamic structure of the UTLS by either enhancing vertical wind shear or reducing static stability (Kunkel et al., 2016; Kaluza et al., 2021; Dörnbrack, 2024) through reversible fluctuations; however, when they dissipate or break, they can induce irreversible mixing and flux convergence, thereby modifying the background flow on longer time scales. These interactions contribute to the formation of an enhanced shear layer in the extratropics so called "tropopause shear layer" (TSL, Kaluza et al., 2021). The TSL is typically identified as the region near the extratropical tropopause where shear exceeds a critical threshold S_t^2, typically the 95$^{\text{th}}$ percentile of climatological dataset. Such pronounced shear is often linked to tropopause disturbances and has been observed on the order of 10^{-2}–$10^{-3}\,\mathrm{s}^{-1}$ (Lane et al., 2004; Kaluza et al., 2021), occurring particularly in dynamically active regions such as jet streaks and frontal zones (Koch et al., 2005; Wang and Zhang, 2007), where clear air turbulence (CAT) is also common. GWs also influence the tropopause inversion layer through wave breaking and momentum deposition, reinforcing its stratification and affecting exchange of air masses between stratosphere and troposphere (or within the lower stratosphere) (Kunkel et al., 2014; Zhang et al., 2015b; Kunkel

et al., 2019). However, a comprehensive analysis of these processes often remain sensitive to model resolution or limited observations and as such pose a challenge for both modeling and observational studies (Plougonven and Zhang, 2014; Stephan et al., 2019a; Geller et al., 2013; Jewtoukoff et al., 2015).

GWs influence tracer transport and mixing in the UTLS by generating turbulence, either through enhanced vertical shear that triggers instabilities like Kelvin–Helmholtz instability or through wave breaking at critical levels where GW phase speed aligns with the background wind (e.g., Shapiro, 1978; Whiteway et al., 2004; Lane and Sharman, 2006). These processes are particularly active in the extratropical transition layer (ExTL), a tracer-defined mixing zone around the tropopause that is prone to cross-isentropic exchange between stratospheric and tropospheric air masses (Hoor et al., 2004; Pan et al., 2006; Hegglin et al., 2009). The ExTL overlaps with the lower part of the lowermost stratosphere (LMS). While the ExTL is situated around the extratropical tropopause, usually defined as an isosurface of potential vorticity, the LMS is the region between the extratropical and the tropical tropopause, bounded above by the 380 K isentrope (Weyland et al., 2025; Appenzeller et al., 1996; Holton et al., 1995; Olsen et al., 2013; Wang and Fu, 2021). The ExTL and LMS are the regions with strong vertical gradients of chemical species which result from the different dynamical and partly chemical processes in the stratosphere and troposphere. In the extratropics, quasi-isentropic transport plays a crucial role for the constituent exchange in the ExTL as has been shown by trajectory-based analyses (Berthet et al., 2007; Hoor et al., 2010) and by airborne observations (e.g., Hoor et al., 2004; Pan et al., 2004; Kunkel et al., 2019). Additionally, small–scale mixing events affects the tracer gradients locally, often in relation to shear instabilities or convection (e.g., Whiteway et al., 2003; Lane et al., 2004; Zhang et al., 2015b; Lachnitt et al., 2023; Dörnbrack et al., 2025).

Observations from aircraft and radiosondes confirm that turbulence in the ExTL enhances vertical mixing of key tracers like ozone and water vapor, affecting UTLS composition and radiative balance (Birner et al., 2002; Birner, 2006; Hoor et al., 2004; Zhang et al., 2015a; Heller et al., 2017). GWs modulate potential vorticity (PV) gradients near the tropopause and drive mixing via shear-induced instabilities (Spreitzer et al., 2019). Beyond its relevance to aviation, CAT also contributes to cross-tropopause transport of chemical constituents and plays a significant role in modulating large–scale atmospheric circulation. Simulations of midlatitude cyclones highlight the role of jet dynamics and GWs in CAT generation (Lane et al., 2004; Trier et al., 2020). In addition to vertical shear–based diagnostics (e.g. gradient Richardson number), empirical turbulence indices such as TI1 and TI2 are widely used in CAT identification (Ellrod and Knapp, 1992; Sharman et al., 2006; Jaeger and Sprenger, 2007). TI1 is a semi-empirical diagnostic; although it neglects the influence of the stratification, it has been shown to perform well within the hierarchy of turbulence predictors (Sharman and Pearson, 2017). Both Ellord indices combine vertical wind shear and horizontal deformation, while TI2 additionally includes a convergence term, enhancing its sensitivity to localized flow features associated with small-scale perturbations. However, forecasting CAT remains challenging due to its intermittent nature and small–scale motion (with turbulent eddies typically spanning horizontal scales of $\sim$10 to 1000 m), compared to the resolution of current numerical weather prediction models (Sharman et al., 2006, 2014; Sharman and Pearson, 2017). More so, it is important to analyse the sources of this turbulence and GW and shear are important larger scale phenomenon for this.

Our primary goal of this study is based on recent revelations from idealized simulations of baroclinic life cycles (Umbarkar and Kunkel, 2025). In these simulations, a clear relation between GW occurrence, enhanced shear and turbulence occurrence

in the lower stratosphere was found. The question is now whether this relation is also evident within an extratropical life cycle over the North Atlantic. First, we present evidence from observations of recent mixing between chemically different air masses during a flight of the WISE (Wave-driven ISentropic Exchange) mission in September 2017. We further examine whether this mixing event is linked to enhanced shear and GW activity (Sect. 3). Second, we examine the representation of shear and the associated GW-induced turbulent mixing in ERA5 reanalysis fields over a larger domain over the North Atlantic during this event in the UTLS (Sect. 4). After that we put our results from the reanalysis data into perspective, once compared to IFS forecast data, and then to ICON forecasts on varying resolutions (Sect. 5). The last point is related to the question which aspects of the GW field can be reliably investigated in ERA5 fields, given their resolution, and whether resolved spectrum of GWs is enough to study their impact on shear and mixing in the UTLS in case studies, and thus potentially may be suited for climatological analyses on this topic. Furthermore, we also investigate whether instabilities triggered by GW-induced shear can lead to the development of CAT.

2 Data and methods

2.1 In situ measurements

In autumn 2017, the WISE (Wave-driven ISentropic Exchange) mission was conducted using the German HALO (High Altitude and Long Range) research aircraft, operating from Oberpfaffenhofen, Germany, and Shannon, Ireland. In this study we focus on research flight 05 (RF05) on 23rd September 2017 between 08:09 and 17:04 UTC. The goal of this flight was to investigate the dynamical and chemical structure of the atmosphere in the vicinity of the tropopause over the North Atlantic between Ireland and a region north of Iceland in a far north reaching subtropical intrusion.

During the WISE campaign, HALO was outfitted with a specialized suite of instruments for in situ and remote sensing. Our analysis is mainly based on in-situ measurement of CO and N_2O from UMAQS (University of Mainz Airborne Quantum Cascade Laser Spectrometer, Müller et al., 2015). For the WISE campaign, the total drift-corrected uncertainty was determined to be 0.94 ppbv for CO and 0.18 ppbv for N_2O (Kunkel et al., 2019). Additionally, we use meteorological parameters measured with BAHAMAS (Basic HALO Measurement and Sensor System, Krautstrunk and Giez, 2012; Kunkel et al., 2019).

2.2 ERA5 reanalysis data

As a reference for the zonal and meridional wind components and as the basis for additional meteorological context, ERA5 the most recent reanalysis produced by the European Center for Medium-Range Weather Forecasts 5th generation (ECMWF, Hersbach et al., 2020) is used. It is based on 4DVar data assimilation and model forecast using cycle Cy41r2 of the ECMWF Integrated Forecasting System model. The model data is available on 137 model levels from the surface to 0.01 hPa with a vertical grid spacing of roughly 300 m in the UTLS. The model level data has further been interpolated on height, pressure and isentropic levels for our analysis. In this study, two ERA5 based products are used: (i) data extracted along the flight path used

in Sect. 3 (Lachnitt, 2025) and (ii) four-dimensional meteorological fields with hourly time resolution and on horizontal grid with 0.25° in latitude and longitude, used in Sect. 4.

2.3 IFS forecast

Next, we use ECMWF IFS operational forecast data as a high resolution companion of the ERA5 reanalysis. The data is based on IFS cycle 43r3 and analyzed on a regular 0.1° latitude-longitude grid with hourly temporal resolution. This data is of interest because the IFS version used to produce this forecast is very close to the version used for ERA5 production. The operational IFS employs a Tco1279 spectral truncation and an associated O1280 octahedral grid which results in an $\Delta x \approx 9$ km grid spacing in the horizontal and incorporates 137 vertical levels which are the same vertical resolution used in reanalysis and in forecasts. This data has almost the same dynamical core and physical package as ERA5 which allows to study the effect of higher horizontal resolution on the representation of the shear and GWs. We use the operational forecast from 23 September 2017 00:00 UTC, with hourly resolution for the first 24 hours.

2.4 ICON forecast

In addition, we use ICON forecast data of this case from Schwenk and Miltenberger (2024). This allows us to study the representation of the same situation in a model with a different dynamical core and physics package as well as in three different resolutions from roughly the resolution in IFS data to almost convection permitting resolution. As such we can directly test how robust our findings are across different model representations. In particular, the atmospheric evolution for this case was simulated using the high resolution ICOsahedral Nonhydrostatic (ICON) modeling framework (version 2.6.2; Zängl et al., 2014) over the North Atlantic Ocean. The simulation was initialized with the operational ICON global analysis at 00:00 UTC

Table 1. Summary of physics parameterization schemes used for ICON simulations

Physics	**Schemes used**
Convection	Tiedtke–Bechtold convection scheme (13 km)
	only shallow convection (6.5 km, 3.3 km)
Non-orographic gravity wave drag	Orr et al. (2010)
Sub-grid scale orographic drag	Lott and Miller (1997)
Turbulence	Raschendorfer (2001)
Radiation	Rapid Radiative Transfer Model
Cloud microphysics	two-moment microphysics (Seifert, 2008)

on 20 September 2017, shortly before the cyclone developed, and ran for 96 hours, ending at 00:00 UTC on 24 September 2017, when the life cycle of cyclone was in its final stage (Schwenk and Miltenberger, 2024). The global ICON model simulation on R03B07 grid (effective resolution of ∼13 km) with a 120 s time step, contained to nested regions using R03B08 (∼6.5

km) and R03B09 (∼3.3 km) grids with 60 s and 30 s time steps, respectively (Fig. A3). In the vertical the ICON simulations have 90 levels from the surface up to 23 km altitude with a vertical grid spacing of roughly 250-300 m in the UTLS. Figure 1 illustrates the ICON nested setup and atmospheric situation over the study region using ERA5 at 11:00 UTC on 23 September 2017. More details about the physics parameterization schemes used for ICON simulations are given in Table 1.

2.5 Deriving resolved gravity wave momentum fluxes and turbulence diagnostics

The GW activity in the model outputs is analyzed via two diagnostic variables: the horizontal divergence $\nabla_h \cdot u_h$ and the absolute momentum flux due to GWs. The model horizontal divergence field is used to identify GW prone regions. Furthermore, in order to understand momentum transport due to small scales and occurrence of GWs, we present the gravity wave vertical fluxes of horizontal momentum in form of probability density functions (PDFs). The vertical transport due to small–scale processes in the extratropical UTLS is investigated via absolute momentum flux (AMF). Here the fluctuations of short-scales from the large–scale background flow are referred to the small–scale perturbations induced by gravity waves (hereafter GW perturbations). Note that the momentum flux at sub-synoptic scales is used here as a first proxy for the momentum flux due to small–scale GWs.

The GW perturbations from synoptic-scale structures are quantified using a hybrid method that combines a dynamical with a statistical approach to separate large and small–scale components of the flow (similar to Wei et al., 2022). We first divide the flow in its divergent and rotational components through the application of a Helmholtz decomposition, i.e., the dynamical approach. For the so called statistical component, we then apply a filter in spectral space using a one-dimensional zonal FFT over the full domain displayed in Fig. 1. With this additional spectral filter we remove the contributions from wavenumber 0 to 20, i.e. $u' = u_{\mathrm{div}} - (u_{\mathrm{div}})_{k \leq k_s}$, where k_s = 20, is the wavenumber cutoff that splits respective quantities into a large–scale and small–scale components. The latter is the perturbation from synoptic-scale structures and is from now on denoted with primes. Note here that sensitivity tests with k_s values of $\pm$ 4 showed no significant variation in the resulting primed quantities. The deviation of small–scale from large–scale flow are shown in Fig. A1. The AMF is then computed from perturbation fields as:

$$\mathrm{AMF} = \rho \sqrt{(\overline{u'w'})^2 + (\overline{v'w'})^2} \tag{1}$$

where ρ is the mean density, and u', v', and w' are the zonal, meridional, and vertical velocity perturbations, respectively. The overline showcasing the perturbation products (i.e. $\overline{u'w'}$ and $\overline{v'w'}$) is computed with a low-pass filtering of the quadratic quantities which uses the same Gaussian spectral filter as in Kruse and Smith (2015).

Recent study by Zhang et al. (2025) suggest that such hybrid scale-separation approaches can be applied at lowermost stratosphere levels (e.g., around 200 hPa). Moreover, Wei et al. (2022); Zhang et al. (2025) further suggest that the use of divergent wind as a proxy for separating GWs provides more reliable estimates of GW momentum flux, particularly in the upper troposphere. Based on this, we emphasize that our hybrid approach for separating synoptic and sub-synoptic scale flow is well justified in the UTLS (Zhang et al., 2025) and follows the commonly used GW scale separation methods as in Lehmann et al. (2012); Wei et al. (2016); Stephan et al. (2019a); Strube et al. (2020); Gupta et al. (2021); Wei et al. (2022); Umbarkar and Kunkel (2025), despite different cutoff wavenumber being used in different studies. Nevertheless, in this study, the focus is

primarily on the lowermost stratosphere, where the scale separation is comparatively more robust, and the limitations of the method are therefore reduced.

Another key diagnostics is the vertical shear:

$$S^2 = \left(\frac{\partial u}{\partial z}\right)^2 + \left(\frac{\partial v}{\partial z}\right)^2. \tag{2}$$

This quantity can also be derived from the wind perturbations and will be denoted as $S^{2'}$ in the following. Turbulence diagnostics and their constituents are computed as outlined in Sharman et al. (2006). The regions with potential for turbulence occurrence are identified via two meteorological parameters: the gradient Richardson number *Ri* and the Ellord turbulence indices, TI1 and TI2. The use of multiple diagnostics is motivated by the need to capture both dynamical and kinematic aspects of turbulence generation in the extratropical UTLS, especially to asses the regions affected by GW-induced shear and mixing. Instabilities being a key prerequisite for mixing of air masses in the atmosphere, such as Kelvin–Helmholtz instability, can be identified using *Ri*,

$$Ri = \frac{N^2}{S^2} = \frac{\left(\frac{g}{\theta}\frac{\partial \theta}{\partial z}\right)}{\left(\frac{\partial u}{\partial z}\right)^2 + \left(\frac{\partial v}{\partial z}\right)^2} \tag{3}$$

i.e., the ratio of static stability (N^2) to vertical wind shear (S^2). Regions with $Ri \leq 0.25$ are theoretically considered to be dynamically unstable and prone to Kelvin–Helmholtz instability. In contrast, when using a value from resolved model quantities, a slightly weaker criterion is often applied and regions with Ri on the order of 1 are considered to be dynamically unstable. Note that the total vertical wind shear is used to compute *Ri*, in order to initially evaluate regions susceptible to turbulence within the baroclinic flow.

While *Ri* captures dynamic instability, it may not fully represent turbulence under complex flow conditions. To account for this limitation, we also employ the Ellord-Knapp turbulence indices, TI1 and TI2, which are empirical diagnostics specifically developed to identify CAT. The Ellord-Knapp Turbulent Index (TI1) has previously been shown to be capable of detecting 70%-84% of CAT occurrences (e.g., Ellrod and Knapp, 1992; Sharman and Pearson, 2017; Kim et al., 2018; Gultepe et al., 2019; Thompson and Schultz, 2021). We resort this to the small scales, ensuring that potential turbulence in the subsequent analysis reflects subgrid or small–scale contributions. It should be noted that Kelvin-Helmholtz instability and turbulence are not explicitly resolved in the used reanalyses as well as forecast even if the GWs themselves are. Instead, these processes are represented through subgrid-scale parameterizations. Our analysis is based on diagnostics of the resolved fields in ERA5, IFS and ICON. These diagnostics highlight regions which have conditions favourable for the occurrence of turbulence. We therefore regard these regions as regions of potential turbulence occurrence based on the resolved fields of the respective model.

TI1 (Ellrod and Knapp, 1992), a well established turbulence indicator combines vertical wind shear perturbations and the total flow deformation (DEF), whereas TI2 adds the contribution from convergence (CVG). The TI1 is calculated using;

$$\mathrm{TI1} = \mathrm{S} \times \mathrm{DEF} \tag{4}$$

whereas, TI2 is derived using;

$$\mathrm{TI2} = \mathrm{S} \times (\mathrm{DEF} + \mathrm{CVG}) \tag{5}$$

where S is the magnitude of vertical wind shear perturbations ($S^{2'}$) as defined in Eq. 2. DEF is the total flow deformation:

$$\mathrm{DEF} = \left(\left(\frac{\partial u}{\partial x} - \frac{\partial v}{\partial y} \right)^2 + \left(\frac{\partial v}{\partial x} + \frac{\partial u}{\partial y} \right)^2 \right)^{1/2} \tag{6}$$

and convergence is calculated according to,

$$\mathrm{CVG} = -\left(\frac{\partial u}{\partial x} + \frac{\partial v}{\partial y} \right) \tag{7}$$

Here, both CVG and DEF are consistently derived from the perturbation wind components (u', v'), and thus TI1 and TI2 are likewise based only on the corresponding prime quantities. The inclusion of CVG in TI2 offers an advantage over TI1 by capturing the small–scale flow features such as those associated with GWs or upper level frontal structures. These region often exhibit enhanced shear and convergence making TI2 more sensitive to turbulence driven by mixing processes.

3 Analysis of GW induced mixing in a baroclinic wave over Iceland

3.1 Meteorological situation

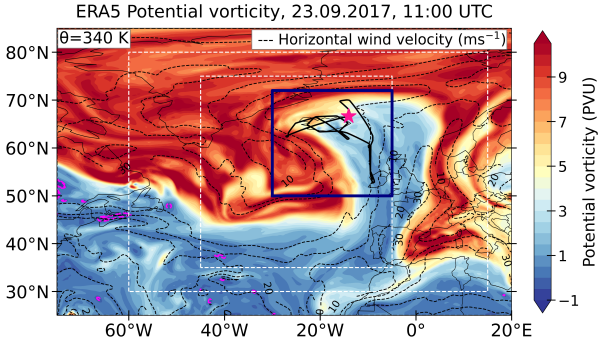


Figure 1. Potential vorticity distribution (in PVU) at the 340 K isentropic surface on 23.09.2017 at 11:00 UTC for ERA5 reanalysis data. The dashed lines show the horizontal wind (in m s^{-1}) on 340 K. The thick black line shows the flight path of RF05 and the star marks the aircraft position at 11:00 UTC. Magenta color shows the negative PV values which are often related to cloud processes.

The major goal of the flight was to determine whether trace species show specific signatures of irreversible mixing in regions of enhanced static stability in the lower stratosphere. We took advantage of this flight data and further ask whether this irreversible mixing event occurs in regions of GW-induced shear enhancement. The flight was planned in the ridge of a synoptic-scale baroclinic wave which evolved during the previous days over the North Atlantic at the edge of large–scale trough.

We start with a description of the atmospheric situation over the North Atlantic during the time which we focus on in the subsequent analysis. The isentropic distribution of potential vorticity (PV) on 340 K in Fig. 1 illustrates the meteorological situation during research flight number 5 of the WISE campaign (in following denoted as WISE RF05) for ERA5 reanalysis fields. The synoptic situation in the UTLS at 11:00 UTC over the North Atlantic Ocean on September 23, 2017 is dominated by the strong meridional excursion of the sub-tropical air masses far north in a region from the Iberian peninsula over Great Britain up to Iceland. The tropospheric streamer is embedded between two equatorward reaching stratospheric streamers, the one to the west being more coherent in its structure, while the one to the east shows more internal structure in terms of its isentropic PV.

The flight went from Shannon, Ireland towards Iceland where a hexagon was flown as well as a dive was performed before returning to Shannon. The flight track is shown by the black line in Fig. 1. The PV distribution shows that the flight took place to a large degree in the region where subtropical air masses, around 11-13 km, moved polewards while some parts of the flight track also reached across the PV gradient into the lower stratosphere. The region of the strong PV gradient corresponding to the location of the jet stream acts as a barrier between tropospheric and stratospheric air masses. On the large–scale, IFS (Fig. A2) and ICON (Fig. A3) forecasts show similar patterns in terms of the overall PV distribution. Moreover, smaller-scale ripple-like structures in the PV field around 20° W and 65° N (Fig. 1) could signify wave activity, which are often generated near jet streams or strong dynamical forcing regions, as reported e.g., for RF07 from WISE (Kunkel et al., 2019). Such small–scale wave like structures in the PV field in the transition region between tropospheric and stratospheric air masses could already hint towards the presence of GWs associated with mixing of air masses. In the next sections we look deeper into the observational data from WISE RF05.

3.2 Identification of flight segments affected by turbulence

We first examine the time series of measured and ERA5 quantities interpolated to the aircraft position during WISE RF05. The goal is to identify regions and periods of potential turbulence and small–scale mixing above the tropopause.

Figure 2 shows a comparison of in situ measured atmospheric state parameters including chemical tracers and potential temperature (a) and instability parameters (b) from the ERA5 reanalysis data that was interpolated in time and space onto the flight path. The pressure measured during WISE RF05 shows that the flight path was designed to ascend with time (Fig 2a). An exception is the dive between 13:00 UTC and 14:00 UTC. This ascent is also mirrored in the decrease of N_2O with time and the associated increase of potential temperature and ERA5 potential vorticity. In contrast, ERA5 vertical shear S^2 and Richardson number Ri show a more diverse temporal evolution. In particular, shear maximizes (up to $\geq 4 \times 10^{-4} s^{-2}$) and Ri shows minima around 11:15 UTC and 13:00 UTC with values below 1 (Fig. 2b). These two time periods are surrounded by times with rather low shear values and high Ri along the flight track. In a next step, we examine these time periods and events in more detail using tracer-tracer correlations.

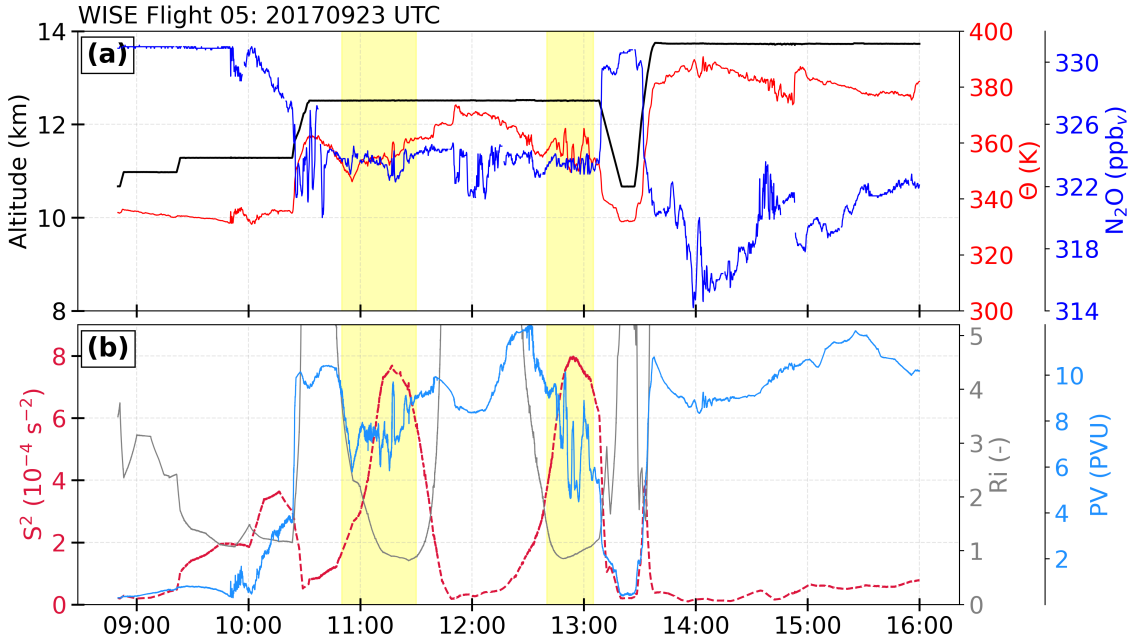


Figure 2. Time series of (a) observed flight altitude (in km, black), potential temperature (in K, red), and nitrous oxide (in ppbv, blue) as well as (b) ERA5 derived quantities along the flight path such as vertical shear (in 10^{-4} s^{-2}, red), Richardson number (dimensionless, grey), and potential vorticity (in PVU, cyan). The light yellow bars and the white bar in between indicate the flight section of the consecutive detailed analysis of mixed air masses.

3.3 Trace gas observations, the role of gravity waves and small–scale mixing

For the identification of small–scale mixing, we examine tracer-tracer correlation based on measurement data. We use trace gases suggesting a tropospheric origin on one side, i.e., CO, and trace species indicative of stratospheric air masses, i.e., N_2O on the other side.

We focus on the time period between 10:45 UTC and 13:05 UTC which is the time period bounded by the two yellow marked regions in Fig. 2. During this time HALO was flying in the LMS with potential temperature values between 330 K and below 380 K. The measurements took place just above the region of the strongest vertical gradients of CO and N_2O where the vertical gradient becomes small again (Fig. 3a, b). Since one would generally expect vertical gradients of N_2O over this potential temperature range, the almost vertical profile is a first indication of a process which mixes or has mixed (i.e. homogenized) air masses prior to the measurements in this altitude range. Additionally, the mixing ratios of CO and N_2O are well below their tropospheric background values, which is also evident in the CO-N_2O correlation (Fig. 3c). The part of the correlation highlighting the time period of interest (marked region) is rather located in the stratospheric branch and partly within the transition region between stratosphere and troposphere. These regions are characterized by low CO and N_2O mixing ratios, with N_2O values below the well-defined tropospheric background of 331 ppbv during WISE RF05 (see also Kunkel et al.,

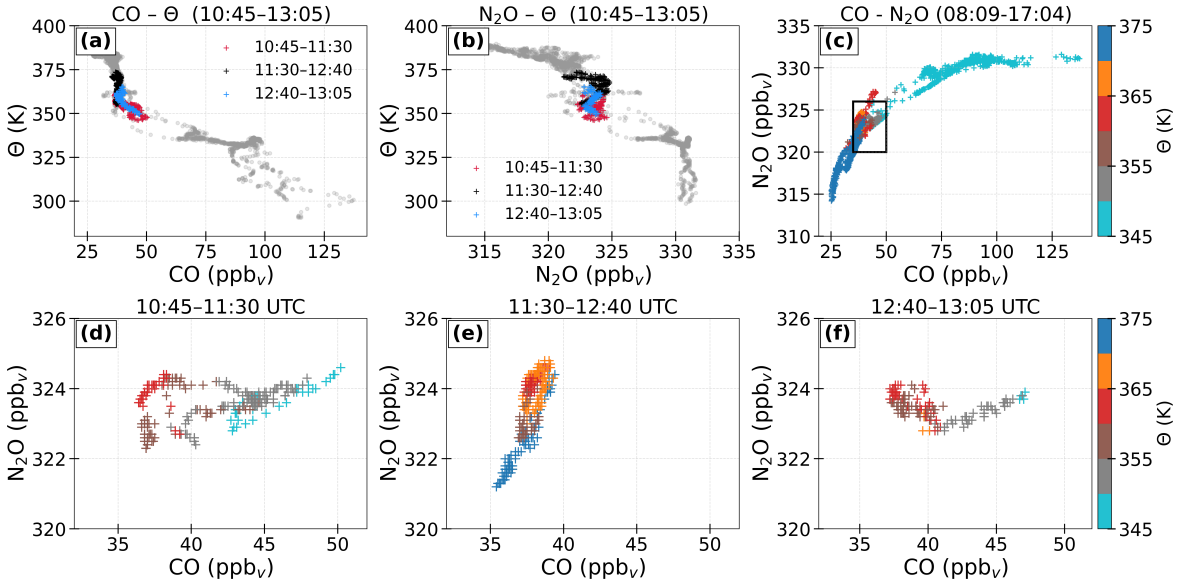


Figure 3. Vertical profiles of (a) CO (in ppbv) and (b) N_2O (in ppbv) with grey circles showing data of the entire flight and color-coded markers indicating the time from 10:45-13:05 UTC. (c-f) Tracer-tracer correlation of the mixing ratios of N_2O and CO for (c) the entire flight and for time periods between (d) 10:45-11:30 UTC, (e) 11:30-12:40 UTC and (f) 12:40-13:05 UTC, color-coded with potential temperature.

2019). Note that irreversible mixing can be followed from the interrelation of CO, N_2O and potential temperature. Due to the chemical life times of the tracers we can infer that N_2O is almost constant in the troposphere with a sink in the upper stratosphere and thus a minor negative gradient with altitude. The same is true for CO, with the difference that the mixing ratios of CO are less constant in the troposphere and the gradient in the stratosphere is stronger due to stronger chemical sink. However, their tracer-tracer relation is positive. More so, we expect to find a monotonic correlation between CO, N_2O and potential temperature Θ. The mixing ratios of CO and N_2O should decrease as an air mass becomes more stratospheric, whereas potential temperature should simultaneously increase. On first glance this relation is evident in the correlation (Fig. 3c) and profiles shown in Fig. 2. While both tracers decrease with altitude, potential temperature increases, which in turn gives specific background relation of these three species. A deviation from the stated background condition is then only possible in the presence of non-conservative processes which also leads to mixing. This is the case here, since deeper inspection of the correlation in the time period of interest, as discussed below, highlights some deviations from this relation. In turn, such deviations can be linked to recent mixing (e.g., Kunkel et al., 2019; Lachnitt et al., 2023).

For further inspection we split the correlation into three time periods: i) 10:45-11:30 UTC (Fig. 3d), ii) 11:30-12:40 UTC (Fig. 3e) and iii) 12:40-13:05 UTC (Fig. 3f). This results in some interesting findings. The first shorter time period exhibits two branches which are interconnected with a mixing line (at around $N_2O \sim 324$ ppbv, $\Theta \sim 359$ K). In the second time period, one branch is evident which shows rather Θ values spread over the entire branch, meaning that no fixed relation between Θ and the tracer is evident although CO and N_2O show a compact positive correlation. In the third time period almost all data points

reside in a very small domain in the correlation space with potential temperature values varying strongly over this domain. All of these findings are potential indications that these air masses have been subject to a process which breaks the relation between CO, N_2O, and Θ; one potential process which can lead to these correlations is mixing. It is interesting to note that the first and third time periods show indications of recent mixing, where the ERA5 analysis shows indications of recent turbulence occurrences (Fig. 2b). Meanwhile, the second time period appears closer to the equilibrated background CO-N_2O relation. This could indicate that the first and third event have been subject to more local recent mixing, while the air mass in between has been mixed some time ago.

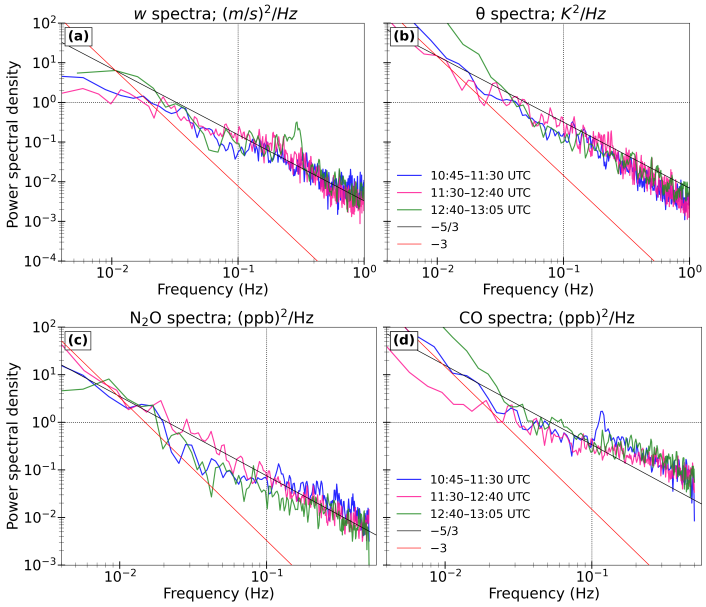


Figure 4. Power spectral densities of (a) measured vertical velocity (in $(m/s)^2/Hz$) and (b) observed potential temperature (in K^2/Hz) from BAHAMAS, and of (c) N_2O (in $ppbv)^2/Hz$) and (d) CO (in $ppbv)^2/Hz$) from UMAQS during WISE RF05 for the time periods 10:45-11:30 UTC (blue lines), 11:30-12:40 UTC (red lines) and 12:40-13:15 UTC (green lines). The orange line indicates the slope of -3 (geostrophic turbulence), the thin black line a slope of -5/3 (mesoscale turbulence).

An analysis of power spectral densities of w, Θ (Fig. 4a, b) and N_2O, CO (Fig. 4c, d) also reveals the presence of small–scale turbulent processes. All spectra rather have a slope of -5/3 which is often seen as an indication for turbulence occurrence on the mesoscale and below (e.g., Zhang et al., 2015a; Dörnbrack et al., 2022; Lachnitt et al., 2023). Particularly, The w spectra shows a slope of -3 for the smaller wavelengths (i.e., for frequency <0.8 Hz), in agreement with Lachnitt et al. (2023). For higher frequencies (shorter wavelengths), the increase of power spectra to 0.5 Hz could be indication of turbulent processes below the synoptic scale. Overall, the w and Θ spectra follows the slope close to $k = -5/3$, can be related to three dimensional isotropic turbulence. This is an indication of dynamic processes on or below the mesoscale affecting the flow. Moreover, N_2O and CO also have a slope close to -5/3 for intermediate frequencies i.e., for smaller wavelengths. From 10^{-2} Hz onward to

larger scales, the N_2O spectra follow a -5/3 slope which suggests that small-scale processes, potentially those related to GWs, contribute to turbulent mixing in the lower stratosphere.

The question on how much GW contribute to the mixing of these air masses is difficult to answer based on the observations along the flight path. Before we broaden our scope in the analysis to the synoptic scale, we further attempt to provide further observational evidence for GWs signatures during the measurements. The close spacings of the measurements shown in Fig. 2 allows the detailed mesoscale structures of the jet/front to be elucidated, including low Ri, and possible coherent phase structures of GWs. Nonetheless, the (time interval) resolution of in situ measurements is too large to properly sample waves with horizontal wavelengths of ∼100 km in hourly model output data. However, the aircraft flew high enough to identify coherent phase lines and/or mixing lines in the lower stratosphere such as those observed in Fig. 3.

Hodographs, which depict the variation of horizontal wind disturbance vectors in velocity space, typically show an elliptical shape in presence of inertia GWs (Hirota and Niki, 1986). Given the high resolution of the measurements, the hodographs can be drawn to identify the presence of inertia GWs and its characteristics (e.g. Guest et al., 2000; Lane et al., 2004; Yoshida et al., 2024). Although, hodographs can be drawn from vertical profiles at a time, given that limited altitude level data, in our analysis a single hodograph is drawn using profiles at multiple times at one flight altitude (e.g., as in Gomes et al., 2025). Figure 5 shows example hodographs for the period of interest where the indication of mixing has been observed. Note that,

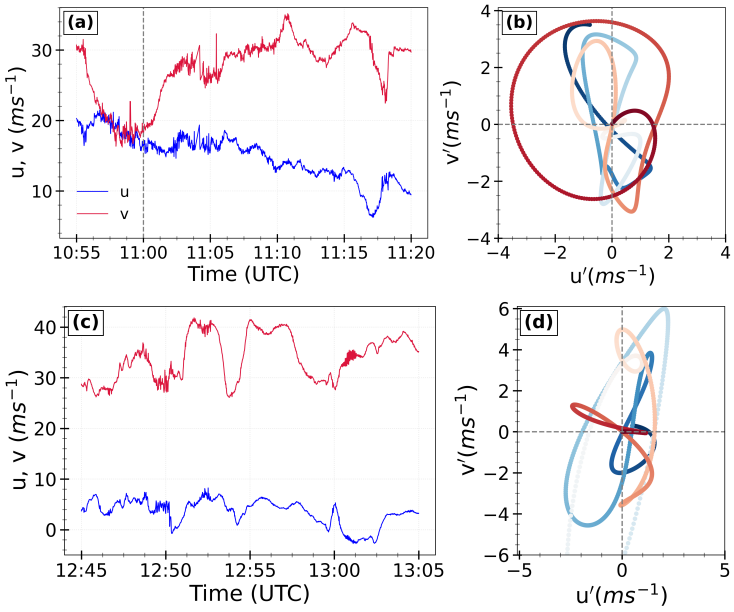


Figure 5. Time series (a, c) of zonal (u, in m s^{-1}; blue) and meridional (v, in m s^{-1}; red) wind component measured during WISE RF05 zoom in for time 10:55-11:20 UTC and 12:45-13:05 UTC. Perturbation hodographs for the corresponding flight period are shown in panels (c) and (d), with trajectories starting in red and ending in blue.

to isolate wind perturbations associated with GWs from the background wind, horizontal wind components (u, v) along the

flight track were bandpass filtered using a 4^{th} order Butterworth filter. The filter was applied to remove both large–scale trends and high-frequency noise, retaining signals within a 2–10 minute period range. The resulting perturbations (u', v') were then used to construct hodographs and to assess wave properties from the in situ measurements. These perturbation time series are shown in Fig. A4. Note that, due to distinct sampling frequency and noise characteristics in the measurements, the flight data is filtered using a 4^{th} order Butterworth bandpass filter (Butterworth, 1930), while the model data is processed using the Helmholtz decomposition approach described in Sect. 2.5, in order to isolate GW related perturbations.

Linear theory of GWs in a uniform background flow predicts that one vertical wavelength of an inertia GW traces an elliptical perturbation hodograph (as described in Guest et al., 2000; Plougonven et al., 2003; Yoshida et al., 2024), which rotates anticyclonically for an upward propagating wave, and cyclonically for a downward propagating wave. This technique has some limitations in terms of conditions with strong background wind shear and hence is only suitable for a part of the wave spectrum with low-frequency, long-wave limit (for more details see Plougonven et al., 2003). This technique is applied to time series of u', v' at $\sim$12.5 km flight altitude. The respective time series of u, v is shown in Fig. 5a and 5c (see also Fig. A4). Of these two selective periods, representing multiple ellipses, only few segments show clear evidence of anticyclonically rotating hodographs, i.e., those line segments colored in red in Fig. 5b, d. A well-defined elliptical pattern is evident in Fig. 5b, indicating the presence of upward-propagating GWs. In contrast, although wave-like oscillations are more prominently observed during 12:45-13:05 UTC (Fig. A4), such a coherent elliptical structure is less apparent in Fig. 5d. Based on this, we focus our subsequent GW-shear analysis around 11:00 UTC and 13:00 UTC, where the wave activity appears most pronounced. Moreover, as we will show later in the analysis of the model data, these profiles give an estimates of at least horizontal wavelength that are similar to those determined from the models. The range of horizontal wavelength estimated is roughly 200-250 km. Also, the limited altitude region here means that only one or two vertical wavelengths are sampled, which adds some uncertainty to the analysis.

Nonetheless, this further motivates an in-depth, model supported analysis to understand whether GWs and GW-induced shear are responsible for observed turbulence and mixing. In the next section, we further investigate this in detail from the model perspectives.

4 Co-occurrence of gravity waves and turbulence in ERA5

In this section we continue our analysis using ERA5 reanalysis fields to examine whether there are indications of GW-induced shear and turbulence. Our primary goal is to first analyze whether there is presence of GWs for the time of our case study over the North Atlantic. We start with the synoptic situation based on ERA5 for the period of interest discussed in Sect. 3.3. In the subsequent sections, we will then explore the relation between these GWs, vertical wind shear and turbulence diagnostics in the lowermost stratosphere. Note that our analysis focuses on the region that includes the entire flight and is defined as 50° N-72° N and 5° W-30° W. The analysis domain is marked in blue in Fig. 1.

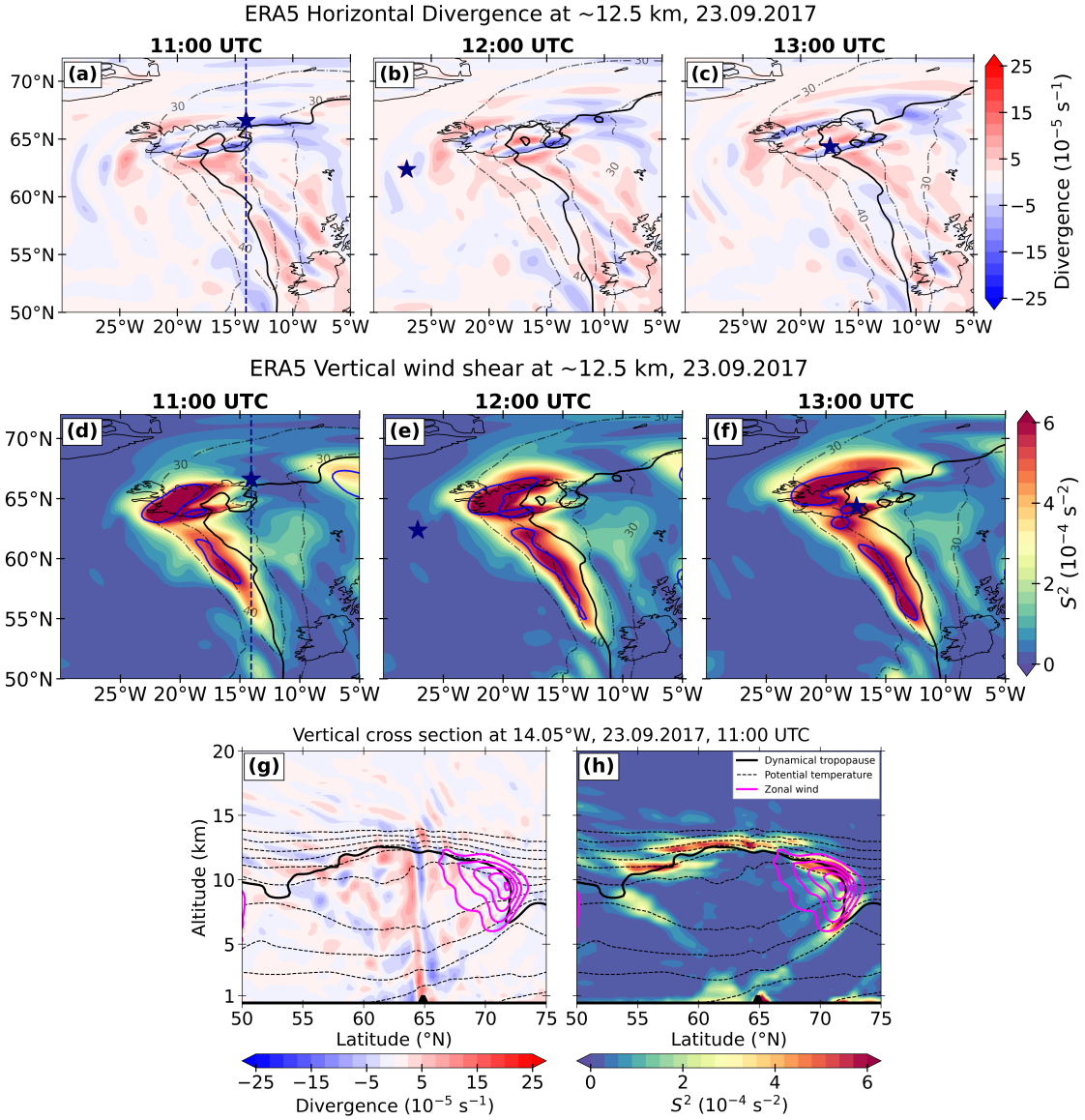


Figure 6. Distribution of horizontal divergence (upper panel) and vertical wind shear (middle panel) at ∼12.5 km altitude for ERA5 reanalysis data at 11:00 UTC (a, d), 12:00 UTC (b, e) and 13:00 UTC (c, f). The dashed lines in upper and middle panels represent corresponding horizontal wind speed for values greater than 30 m s^{-1}. The RF05 flight location during the time shown by blue star. The vertical cross sections of divergence (g) and shear (h) at 14.05° W during 11:00 UTC is shown in lower panel. The solid black line represent the 3.5 PVU as a dynamical tropopause whereas dotted lines in lower panel represent the potential temperature starting from 280 K (bottom) to 380 K (top) with 10 K increments. Magenta contours in (g, h) denote zonal wind speed (20, 30, 40, 50) in m s^{-1} and solid blue lines in middle panel represent $Ri = 1$.

4.1 Analysis of gravity waves and vertical shear

We start with the horizontal divergence field to identify location and characteristics of potential GW signatures in the lowermost stratosphere. We define the extratropical tropopause based on the dynamical tropopause definition with a value of 3.5 PVU (1 PVU=1×10^{-6} K m^2 kg^{-1} s^{-1}).

Figure 6a-c shows the horizontal divergence at 12.5 km ($\sim$ 200 hPa) for ERA5 reanalysis data between 11:00 and 13:00 UTC. The alternating signatures of divergence-convergence observed in horizontal divergence field, representing presence of GWs features, are evident near the jet streak exit region with enhanced activity between 60° N-72° N, particularly over and to the east of Iceland along the flight track (Fig. 6a). This GW field is primary noticeable over the Icelandic highlands. The flow associated with the baroclinic system over the topography of Iceland leads to the emission of the GWs. Its signal is already evident in the troposphere and changes its appearance in term of wavelength over the tropopause. This change is expected due to changes in stability across the tropopause. The flow over orography appears to be source mechanism for the generation of GWs, particularly given that the GW signal occurs near the transition between ocean and Icelandic topography. The horizontal divergence field further reveals the emergence and evolution of GWs, along with associated wave-induced features at later times. These waves generated over Iceland evolve within the ridge of the upper-tropospheric jet stream around 67° N (Fig. 6c). Horizontal wavelength of this waves is on the order of hundred kilometers that is similar to wavelengths of inertia GWs. On the large scale, however, all time steps exhibit similar divergence patterns with slight changes in both amplitude and orientation, reflecting a systematic evolution of the wave field. Overall, this indicate that GWs has their source of imbalances in the synoptic flow and propagate into the lower stratosphere during their evolution.

The corresponding vertical cross section of horizontal divergence at 14.05° W representing the approximate flight location at 11:00 UTC (marked by the dashed line) is shown in Fig. 6g. The thick solid line marks the dynamical tropopause, however, the GW activity influence this. The undulations in the PV field are the signatures of upward propagating GWs, with wave amplitudes extending through the lower stratosphere. Moreover, there is presence of upward propagating wave signatures with short horizontal wavelength that are excited in the upper troposphere above the location of troposphere jet. This indicates that the GWs that are originated from surface orography further emitted away from their source region and propagate upward toward the lowermost stratosphere. The observed wave packet propagates only a short horizontal distance, while spanning vertically up to $\sim$17.5 km in altitude, suggesting a low ground-based phase speed and a narrower vertical wavelength. It is also important to note that, over 14.05° W, GW characteristics vary in its amplitude and wavelength with time, but shows spatially and temporally persistent GW signatures at this region (see also Fig. B1).

Of interest is the fact that ERA5 despite its lower horizontal resolution, is able to capture the appearance of GWs in the LMS. This is consistent with findings of previous studies that have investigated GWs in ECMWF products and reanalyses in particular (see Jewtoukoff et al., 2015, and references therein). Horizontally propagating GWs with large horizontal wavelengths tend to dominate the horizontal derivatives of momentum fluxes, whereas, upward-propagating large-amplitude GWs (i.e., with large vertical wavelength) carry large momentum, which then contribute to the vertical derivatives of the wind components across the tropopause. This, in turn, leads to higher shear values and lower Richardson numbers, that increases the probability of

turbulence in this region. We now move our discussion to an analysis of vertical wind shear, a key prerequisite for dynamical instability and thus turbulence related to observed GWs.

Figure 6d-f shows the distribution of vertical shear of horizontal wind at 12.5 km ($\sim$ 200 hPa) for ERA5 reanalysis data between 11:00 UTC and 13:00 UTC. We see significant shear north of 60° N in the vicinity of GW activity identified earlier from the horizontal divergence field, i.e., around 65° N and 15° W. As discussed in the paragraph above, ERA5 shows prominent signs of GW activity across the tropopause region and in the lower stratosphere, being an interesting region to further study the GWs role to shear enhancement. Moreover, the jet location and dynamical tropopause in Fig. 6d-f holds important piece of information about the jet disturbances being one of the source region of high shear abundance in this region, particularly around the tropopause fold at around 70° N. Reduced *Ri* values (in blue) are observed in the vicinity of the jet exit region, suggest a widespread potential for the occurrence of dynamic instability. Notable feature is that *Ri* show low values almost in all regions of enhanced shear. In particular, the spatial and temporal evolution of synoptic flow show co-location of shear with GW patterns in the lowermost stratosphere (Fig. 6a-f).

Furthermore, the vertical distribution of shear at 14.05° W (Fig. 6h) indicate the maximum shear abundance in the ridge and along the tropopause fold with maximum values reaching up to $6 \times 10^{-4}\mathrm{s}^{-2}$. The maxima in the ridge (around 64° N) is in the proximity of GWs which in turn could affect the shear values there. These shear maxima is observed near the regions of GWs likely above the lifted air masses reaching up to the tropopause and beyond. Particularly, in the UTLS, the jet-stream on larger scales and GW on smaller scales contribute significantly to the generation of shear. Also, there is countable co-location of shear on large scale and shear perturbations on smaller scale (see Fig. B2a) with GW patterns across the tropopause (Fig. 6d-f) and thus the shear location related to the phase of GWs modes remain consistent in vertical distribution. Overall, the upward propagating GW signals observed across the tropopause in ERA5, indicate a spatiotemporal co-occurrence of GWs and vertical wind shear.

However, this requires further investigation to understand whether the small–scale, vertically propagating GWs observed in ERA5 are of relevance to the shear generation across the tropopause. One possible explanation for this is that vertically propagating, large amplitude, high vertical (short horizontal) wavelength GWs locally modulate the N^2 in the LMS (Kunkel et al., 2014; Kaluza et al., 2019; Zhang et al., 2019), which in turn also allows to accumulate vertical shear in this region. This suggests that GWs may contribute (or influenced) partially to the vertical shear generation in the lower stratosphere. On the other hand, the maximum shear in locations other than GW activity, likely generated from the large–scale components including the jet stream or baroclinic disturbance. This further motivates a deeper look at the significance of small–scale GWs to high wind shear, and subsequently to the potential turbulence occurrence.

4.2 Turbulence diagnostics in the LMS

In continuation to turbulence analysis, this section addresses the occurrence of dynamic instability associated with GWs, particularly in the LMS, as well as the relation between the occurrences of GWs and shear perturbations.

To understand the potential occurrence of turbulence associated with GWs and shear, we start with two-dimensional probability density distribution of the AMF and the vertical shear perturbations. The color shows the relative frequency of AMF and $S^{2'}$

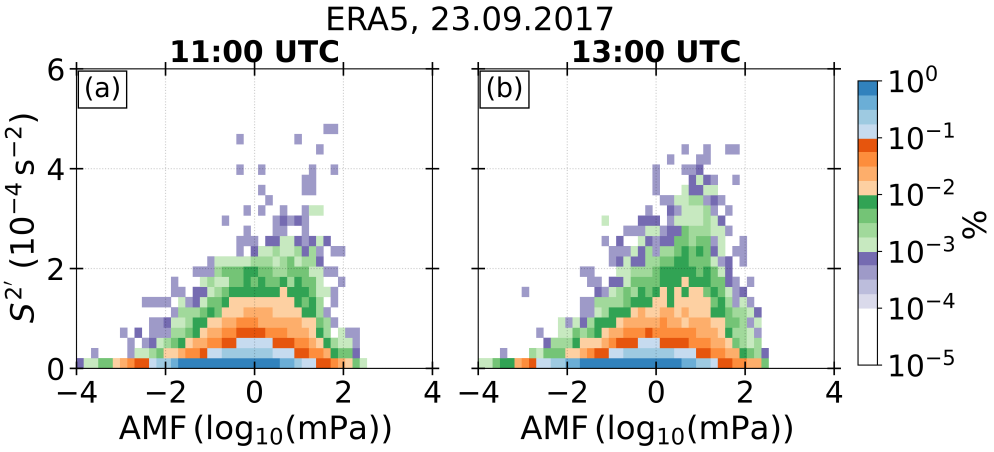


Figure 7. Relative occurrence frequency distribution of absolute momentum flux due to GWs-vertical shear perturbations pair in the LMS for $0 \leq Ri \leq 1$ for ERA5 reanalysis data at 11:00 UTC (a) and 13:00 UTC (b). Normalized counts of PDF distribution is shown. Logarithmic occurrence frequency color scale is applied.

in the LMS with respect to low Ri (i.e, $0 \leq Ri \leq 1$, Fig. 7). Note also that the occurrences are retrieved over flight covered region (50°N–72°N, 5°W–30°W, i.e., blue box in Fig. 1). We use AMF as it is one of the metrics used to quantify momentum transport due to GWs. One would expect momentum-flux deposition by GWs in the region where GW-induced instability and turbulence occur (Fritts and Alexander, 2003). Besides this, since turbulence is relatively rare event under general atmospheric condition (Sharman et al., 2012; Dörnbrack et al., 2022), only a few data points are anticipated during episodes of potential turbulence in the LMS.

If smaller scales play a major role, we expect a positive correlation between small–scale absolute momentum flux and shear perturbations in terms of turbulence occurrence in the LMS. Qualitatively, we already notice a positive correlation between shear abundances and GWs in the LMS during an event of potential turbulence occurrence, i.e., $0 \leq Ri \leq 1$ in ERA5 (Fig. 7). Here, the $S^{2'}$ occurrences and maxima reach up to $5 \times 10^{-4} s^{-2}$, where AMF maximum is in order of 10^2 mPa. Note here that a quite similar relation is evident at 11:00 UTC and 13:00 UTC, when looked at the higher occurrences within the range of 10^{-3} to 10^{-1} (see orange and green colors). The observed slight changes in the occurrences may depend on the underlying flow conditions. We interpret this co-occurrences as an indication that the small-scales and, especially GWs, contribute substantially to the occurrence of pronounced large- as well as small-scale shear and potential turbulence in the LMS. Overall, this result supports previous analysis based on idealized studies in terms of GWs related to the shear and subsequent turbulence (Umbarkar and Kunkel, 2025).

As discussed previously in Sect. 4.1, ERA5 represents the resolved fine scale structures of the GWs, and here, as such shows the positive correlation between AMF and shear fluctuations (Fig. 7). It will be interesting to see in a follow-up analysis whether this is limited to ERA5 modeling systems or to our case study. Overall, these results pinpoints the crucial role of GW-induced shear to the potential turbulence occurrence, and subsequently representing the important role of GWs to transporting the

momentum across the tropopause.

We now turn the attention to the small–scale behavior of GWs, as the GW-induced shear can coincide with the regions of considerable dynamic instability and potentially influence turbulent mixing. The following section examines CAT and its spatial relation to GWs.

4.3 Are these GWs responsible for CAT occurrence?

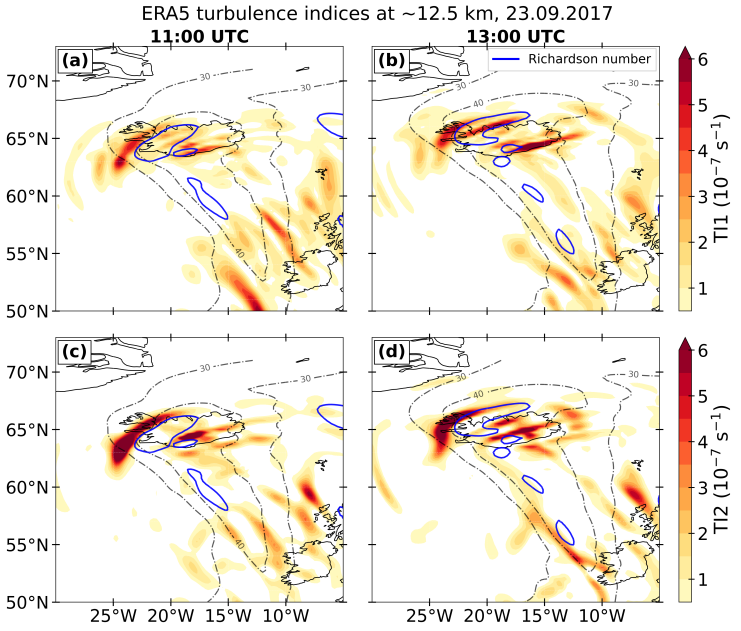


Figure 8. Distribution of turbulent indices TI1 (a, b) and TI2 (c, d) at ~12.5 km altitude for ERA5 reanalysis data at 11:00 UTC and 13:00 UTC. The dashed black lines presents the horizontal wind speed >30 $\mathrm{m\,s^{-1}}$ and blue contours denote $Ri \leq 1$.

One previously suggested impact from dynamic instability is that any associated inertia GWs could lead to CAT when these waves breaks (Knox, 1997). Previously, Thompson and Schultz (2021) showed the emission of inertia GWs, following the release of dynamic instability, instigate light–moderate occurrences of CAT around the unstable region using idealized model simulations. We widen our analysis by examining both the broader upstream flow patterns and the small–scale disturbances, primarily GWs, that contribute to the development of dynamical instability and potentially to the CAT occurrences in the lower stratosphere.

Turbulence does not develop as a single continuous area, but in sporadic pockets of light to moderate intensity that persists for few minutes around the periphery of unstable region (Sharman et al., 2006). Our results from small–scale contribution show a similar pattern (see Fig. 8). While ERA5 data have an hourly resolution and may limit the representation of such short lived events, the observed structures suggest the conditions conducive to their occurrence, albeit with reduced intensity. As the GWs propagate upward through the tropopause, the wave perturbations significantly modify the local Ri, with the apparent $Ri \leq 1$

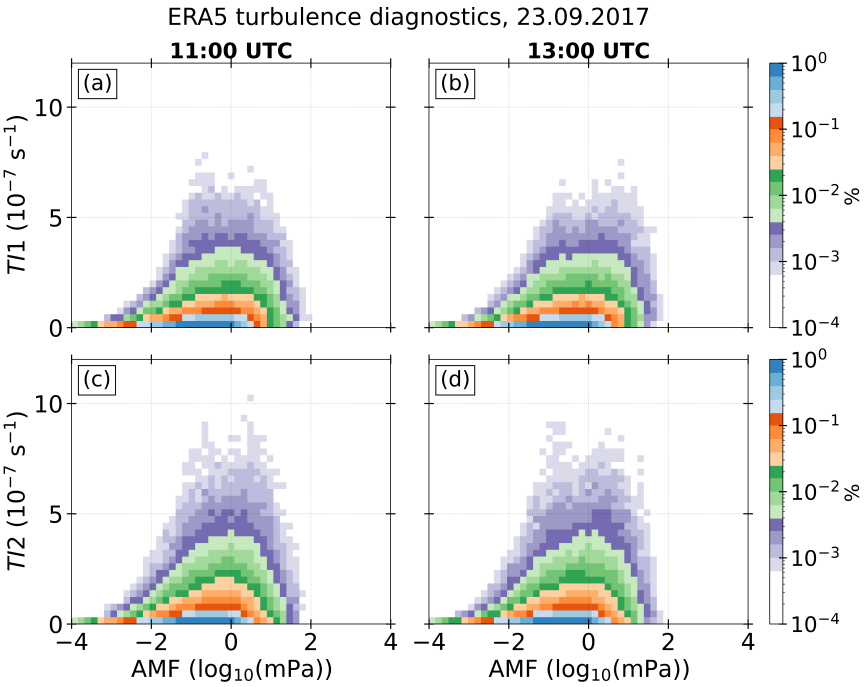


Figure 9. Frequency (%) distribution of absolute momentum flux-turbulent indices TI1 (a, b), TI2 (c, d) in pairs over the LMS for ERA5 reanalysis data at 11:00 UTC and 13:00 UTC. Normalized counts of PDF distribution is shown. Logarithmic occurrence frequency color scale is applied.

bands are the regions of possible Kelvin-Helmholtz instability (Fig. 8). Subsequently, along the phase lines of GWs, there are apparent bands of enhanced TI1 (Fig. 8a, b) as well as TI2 (Fig. 8c, d) in the lowermost stratosphere. The enhanced turbulence, especially the CAT was due to the small–scale GWs and it is proposed that such mechanism contributed to the turbulence encountered during the flight.

Calculating the TI1 index as a proxy for CAT from zonal and meridional wind perturbations (u', v'), we find several regions where CAT develops simultaneously across the tropopause. Given that the current study focus on the occurrence frequency of CAT in the UTLS likely near the upper level jet stream, we choose the 95th percentile value of the total occurrences as the thresholds of each CAT index for light-moderate intensity level following Lee et al. (2019, 2022). Figure C1 illustrates the frequency distribution of CAT indices over the LMS. For ERA5, the resulting threshold values for TI1 and TI2 are $1.4 \times 10^{-7} s^{-1}$ and $1.5 \times 10^{-7} s^{-1}$, respectively (see also Appendix C).

Collating all turbulence occurrence throughout the simulation, we find that most occurrences fall into this light–moderate category, but some occurrences of moderate intensity are also found (Fig. C1a). Nonetheless, the moderate to greater intensity CAT in TI1 with slightly less occurrences are strong in the positive tail of TI2 (Fig. C1b). The more pronounced moderate-level CAT with GWs formulation, i.e., TI2 (see Fig. C1b), hints at probable contribution of GWs to CAT development. One possible

explanation for this could be that GWs over Iceland observed in the ERA5 lead to the maximum shear perturbations as well as pronounced TI1 and TI2, which further induce strong potential instability and ultimately result in the development of CAT. Figure 9 show the 2D probability distribution of TI1-AMF and TI2-AMF pairs in the LMS domain. Moreover, as discussed above, if the subgrid or small-scales plays a major role, the positive relation between AMF and turbulent indices is expected. When we investigate this relation in the LMS, we observed the positive correlation between occurrence frequencies of these two quantities. There are only slight variations in terms of occurrences of maxima of TI1 and TI2 in the LMS (Fig. 9). The TI1 shows smaller values in terms of abundance of TI1 and AMF above the threshold ($\sim 7.5 \times 10^{-7} s^{-1}$), indicating light to moderate level CAT (Fig. 9a, b). In this case, the TI2 shows slightly higher occurrence frequencies than the TI1, with the maxima reaching moderate intensity CAT ($\sim 10 \times 10^{-7} s^{-1}$) (Fig. 9c, d).

Overall, following the positive relation between small-scale shear and AMF in the LMS above the North Atlantic (Sect. 4.3), we can go even one step further. The co-occurrence of enhanced AMF with both increased shear and elevated turbulence indices, TI1 and TI2, leads us to the conclusion that GW play a role for the occurrence of CAT in our analysis region.

Combining all these information pinpoints the crucial role of GW-induced shear to the potential turbulence occurrence, and subsequently representing the important role of GWs to transporting the momentum across the tropopause. Nonetheless, ERA5, despite its coarser horizontal resolution, captures a larger portion of GW spectrum providing valuable information on the spectral characteristics of GWs.

In conclusion, the results obtained in Umbarkar and Kunkel (2025) from the idealized cases are also evident in the "real" world in the ERA5 perspective. As of now, the discussion centred around the role of GWs in the occurrence of strong shear in the LMS, and whether potential turbulence occur in the region of the GW-induced shear in ERA5. In the next section, discussion focuses on sensitivity analysis, that is a comparison for an ECMWF product with finer horizontal grid resolution. Moreover, it is yet to investigate whether this findings are also true in the real world that uses non-hydrostatic dynamical core.

5 Sensitivity analysis: gravity waves and turbulence occurrences in IFS and ICON

Analysis of ERA5 reanalysis revealed the plausible role of GWs to generation of shear and potential turbulence based on dynamical processes. In this section, we further examine how GWs emerge in finer horizontal grid resolution and how the occurrence, location, and properties of GWs are influenced by the horizontal grid spacing in the UTLS. From here onward, we focus on the 11:00 UTC time step; but the analysis at 13:00 UTC would result in the same conclusions in terms of the role of GWs in shear and potential turbulence in the UTLS.

5.1 Analysis of GW, shear and turbulence in the IFS

First, we aim to assess the resolution dependence for which we use IFS forecast with finer spatial resolution than that of ERA5. On the larger scale, the evolution of the synoptic flow is similar to ERA5 discussed in Sect. 4.1. However, slight deviations are evident in mesoscale features as well as location of GW structures (Fig. 10). These similarities and differences are highlighted in Fig. 10a which illustrates distribution of horizontal divergence and shear at 12.5 km altitude. IFS captures finer horizontal

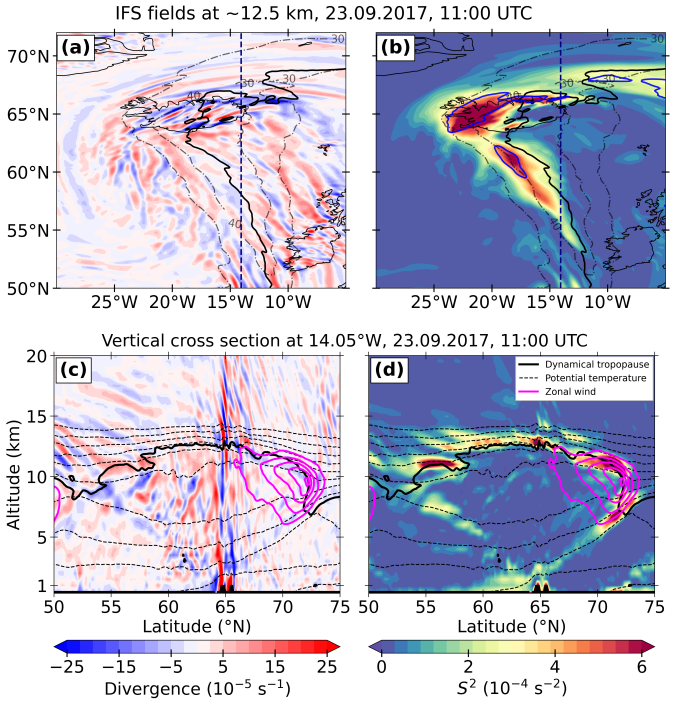


Figure 10. Distribution of horizontal divergence (a) and vertical wind shear (b) at ∼12.5 km altitude for IFS data at 11:00 UTC. The dashed lines in upper and middle panels represent corresponding horizontal wind speed for values greater than 30 m s^{-1}. The RF05 flight location during the time shown by blue star. The vertical cross sections of divergence (c) and shear (d) at 14.05° W during 11:00 UTC is shown in bottom panel. The solid black line represent the 3.5 PVU as a dynamical tropopause whereas dotted lines in lower panel represent the potential temperature starting from 280 K (bottom) to 380 K (top) with 10 K increments. Magenta contours in (g, h) denote zonal wind speed (20, 30, 40, 50) in m s^{-1} and solid blue lines in (c) represent the $Ri = 1$.

structures of divergence, indicative of GWs activity covering Iceland with moderate amplitudes in the northwestern sector, rather with larger amplitude small–scale features. That is to say, IFS reveals prominent, though small magnitude GWs over the region of northeastern highlands of Iceland, features that are not clearly captured in ERA5. Notably, this region lies along the flight path where signatures of mixing are observed. The corresponding vertical distribution at 14° W shows a packet of GW propagating upward into the lower stratosphere, with a relatively larger vertical wavelength (∼2-3 km) and short horizontal (∼100 km) wavelength (Fig. 10c). This reveals the presence of much more finer-scale structures in IFS, whereas such features are less pronounced in ERA5 (see also Fig. 6g). This indicates that GWs characteristics, especially their horizontal details, are strongly dependent on the spatial resolution. Overall, these differences suggest that the nominal resolution largely controls the magnitude of the GW fluctuations in both reanalyses and forecasts.

Analysis of vertical shear (Fig. 10c) at the same altitude reveals high shear values around 60–65° N over the northwestern part of Iceland, especially in the proximity of GWs observed earlier. As discussed in the paragraph above, IFS shows much more fine signatures of GWs in the lower stratosphere than ERA5, and as such it is interesting to further study the GWs role to

shear enhancement. More prominent regions of $Ri \leq 1$ (in blue) are observed in the vicinity of jet stream. This hints at shear generated from jet disturbances being susceptible to potential turbulence in this region. Altogether, these are similar regions of co-location of intense GWs and pronounced shear that are identified in ERA5. At the same time, the vertical distribution of shear shows maximum (up to $6 \times 10^{-4} s^{-2}$) abundance just above the tropopause, where GWs propagate along the PV gradients of the streamer. The region of shear maximum around 65° N is also the region of GW activity that are originated from surface topography, and thus could contribute to the enhanced shear in this region. Although the IFS exhibits a pattern of S^2 that closely resembles that of ERA5, the spatial scale of the maxima is notably smaller in the vicinity of the ridge. Overall, IFS shows a similar but more pronounced co-location of shear with GW patterns compared to ERA5 and further indicate a spatiotemporal co-occurrence of GWs and vertical shear.

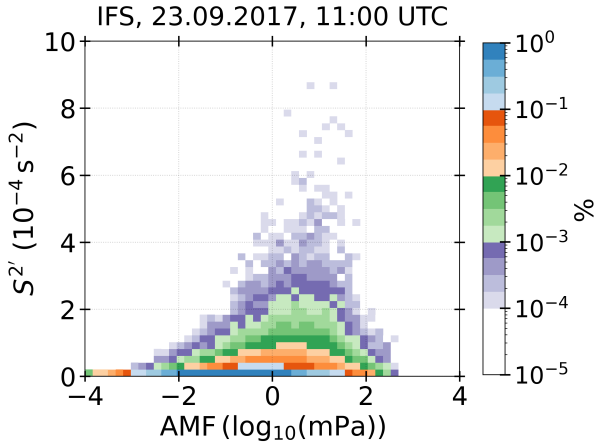


Figure 11. Same as Fig. 7 but for IFS at 11:00 UTC.

To address the occurrence of dynamic instability associated with GWs in the LMS in IFS, we now move our discussion to the occurrence frequency distribution of AMF-vertical shear perturbations for low Richardson numbers between 0 and 1. Since IFS resolve vertical shear similar to ERA5 reanalysis and exhibits a comparable pattern of GWs and S^2, here, we can expect a similar positive correlation between AMF and S^2 in the LMS. Based on this, we find the positive correlation between AMF and shear fluctuations in the IFS, albeit with higher occurrences at the range of 10^{-3} to 10^{-2} (see the green colors, Fig. 11). Here, high resolution IFS likely shows more pronounced $S^{2'}$ and AMF than ERA5 likely due to finer resolution (Fig. 7). These co-occurrence frequencies are about an order of magnitude larger than ERA5. This also hints at better represented GWs in IFS than in ERA5. In IFS, we note that shear perturbations are more patchy and shows colocation with GWs in general (see also Fig. B2b). The occurrence of high shear in regions frequently exposed to enhanced GW activity suggests that well-resolved GW features contribute to the occurrence of strong shear and thereby to the potential turbulence in the LMS.

The higher occurrences of GWs and shear perturbations in the IFS owe their potential importance to the fact that both features could contribute potentially to moderate CAT occurrences in the LMS. In this regard, Fig. 12 show the bands of high TI1 and TI2 along the phase line of GWs, which are more prominent in IFS when compared to ERA5 (8). There are also apparent

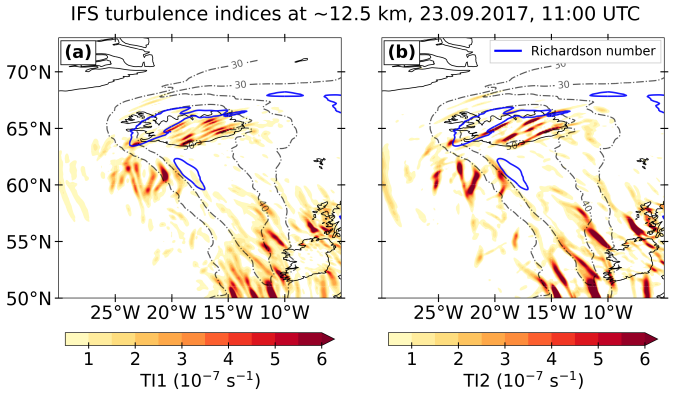


Figure 12. Distribution of turbulent indices TI1 (a) and TI2 (b) at ∼12.5 km altitude for IFS. The dashed black lines presents the horizontal wind speed $> 30\,\mathrm{m\,s^{-1}}$ and blue contours denote $Ri = 1$.

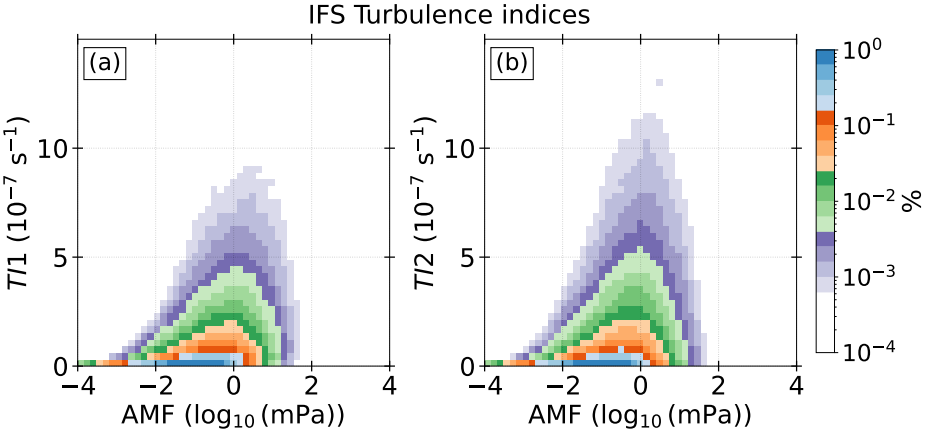


Figure 13. Frequency (%) distribution of absolute momentum flux-turbulent indices TI1 (a), TI2 (b) in pairs over the LMS for IFS data. Normalized counts of PDF distribution is shown. Logarithmic occurrence frequency color scale is applied.

localized volumes of small–scale turbulence formed in the bands of the reduced Ri. The threshold values for TI1 and TI2 selected based on the 95th percentile criterion are $2.1 \times 10^{-7} s^{-1}$ and $2.45 \times 10^{-7} s^{-1}$, respectively (Fig. C1). Following this, Fig. 13 continues to demonstrate the distribution of TI1-AMF and TI2-AMF pairs in the LMS domain. The positive relation between AMF and turbulent indices is evident from the occurrence frequencies of these two quantities. When compared with its predecessor, IFS shows similarity in terms of occurrences of TI1 (Fig. 13a), rather with slightly higher occurrence reaching up to light to moderate level CAT. When looking at the TI2, while ERA5 shows slightly less occurrence in this case, its maxima reaches moderate intensity CAT in IFS (Fig. 13b). This reveals that GW play a role for the occurrence of CAT and further highlights the necessity to properly simulate GWs and to capture small-scale processes considering suitable higher spatial resolution.

Until now, the discussion in this section centred around the role of GWs in the occurrence of strong shear in the LMS, and whether (clear-air) turbulence occur in the region of the GW-induced shear across available datasets from ECMWF, that uses hydrostatic dynamical core in combination with semi-implicit and semi-Lagrangian numerical schemes. Finally, we want to investigate whether this findings are also true for ICON simulations of this case. This could provide a unique insight into the situation, since we have the same situation in three model domains (with and without convective parameterization) and also in relation to our previous results from idealized ICON model simulations (Umbarkar and Kunkel, 2025).

5.2 Analysis of GW, shear and turbulence in the ICON

The dynamical situation previously examined using ECMWF products is further evaluated in this section using ICON simulations with varying horizontal resolutions and physics parameterization schemes. The ICON simulations differ not only in domain configuration but also in time step and convection schemes used. More details about the simulations and physical parametrization schemes used for this simulations are given in Sect. 2.4.

We start again with the distribution of horizontal divergence at 12.5 km altitude (Fig. 14). The pronounced GW activity over the northeastern Icelandic highlands is evident across all domains (Fig. 14a–c), with enhanced GW signatures between 60° N-72° N, particularly over and to the east of Iceland along the flight track. The ICON simulation with $\Delta x \approx 3.3$ km captures GW activity across the analysis domain with moderate wave activity in the northwestern sector (Fig. 14c), albeit with large amplitude small-scale wave features. Of interest is the fact that, ICON with ≈ 6.5 km grid spacing reveal prominent, though small magnitude, upward propagating GWs that persist similar characteristics of IFS, and are the features that are not clearly captured in ERA5 (see also Fig.B3). Moreover, ICON ≈ 13 km shows a similar vertical structure to IFS, with a slightly shorter vertical wavelength of $\sim$3 km, while spanning vertically up to $\sim$17.5 km in altitude (Fig. B3a). In contrast, the finer resolution (Fig. B3c) shows more prominent wave properties with large amplitude and large vertical wavelength propagating upwards and features extend beyond $\sim$19 km in vertical. However, it should be noted that the shallow convection scheme used for the nested domains, i.e., for $\Delta x \approx 6.5$ and $\Delta x \approx 3.3$ km, could be a source for different signatures with smaller scales. All three domain clearly exhibit a more pronounced GW signatures with resolved finer scales, with slight changes evident in both amplitude and magnitude of GWs. Moreover, the appearance and occurrence of GWs as well as small-scale features are highly dependent on the model grid spacing and convection processes implemented therein.

The corresponding horizontal distribution of vertical shear (Fig. 14d–f), shows higher shear abundance in the vicinity of GW activity identified earlier at around 65° N and 14° W. Here again, the $\Delta x \approx 3.3$ km resolution captures finer details and shows high shear values. This more enhanced shear is colocated with pronounced GW activity identified earlier across the tropopause region and in the lower stratosphere (see also Fig. B3d-f). It should however noted that enhanced GW activity in higher resolution experiments likely originated from convective sources and thereby could lead to higher shear abundance in the lower stratosphere. Moreover, this overall behaviour indicates that both horizontal and temporal resolution substantially influence the magnitude and representation of GW fluctuations in the forecasts, consistent with the findings presented in Sect. 5.1. This highlights the need to properly simulate GWs and to effectively capture small-scale processes accounting suitable higher spatial resolution.

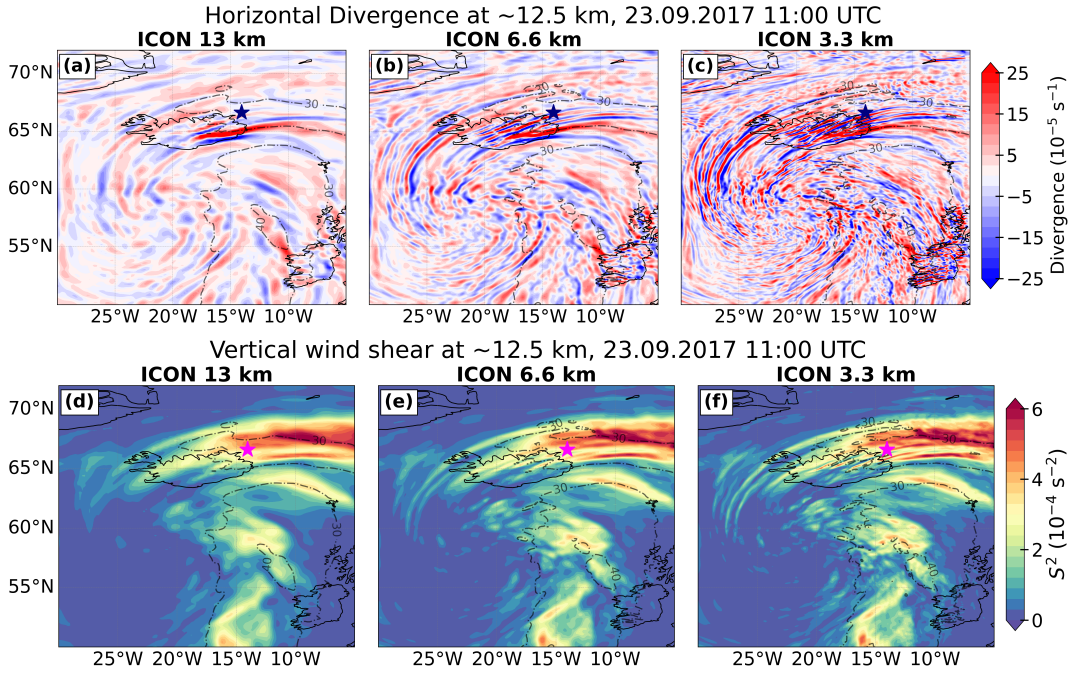


Figure 14. Distribution of horizontal divergence (upper panel) and vertical wind shear (lower panel) at 12.5 km altitude for ICON 13 km, 6.5 km and 3.3 km resolution nested simulations overlaid with flight location at 11:00 UTC shown by star. The dashed line represent corresponding horizontal wind speed for values greater than 30 ms^{-1}.

Diagnostics of potential turbulence and CAT in the LMS

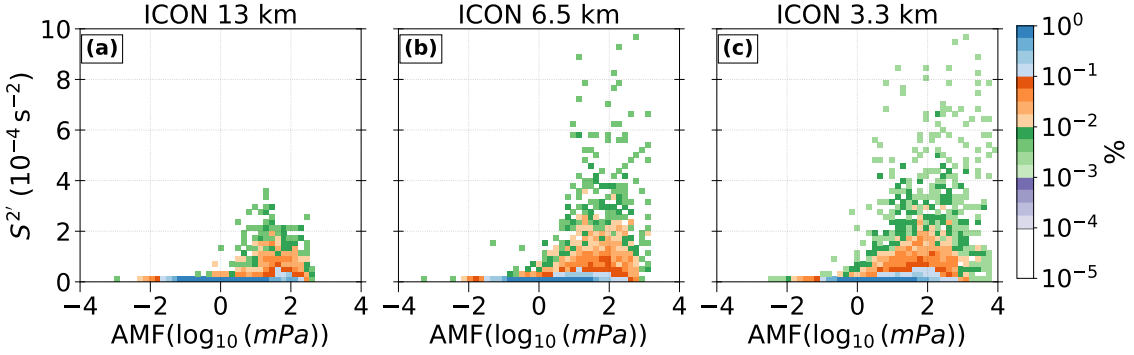


Figure 15. Relative occurrence frequency distribution of absolute momentum flux due to GWs-vertical shear perturbations pair in the LMS for $0 \leq Ri \leq 1$ for ICON 13 km, 6.5 km and 3.3 km resolution nested simulations at 11:00 UTC. Normalized counts of PDFs distribution is shown. Logarithmic occurrence frequency color scale is applied.

To further investigate the previously identified close relationship between momentum flux and shear perturbations in the context of turbulence occurrence within the LMS, both AMF and S^2 quantities are masked for the regions in the LMS where potential turbulence (i.e., $0 \leq Ri \leq 1$) could occur. A closer examination reveals that enhanced shear occurrences are predominantly associated with AMF values on the order of 10^1–10^3, i.e., corresponding to a range from a few to a few hundreds of millipascals (see Fig. 15). Also, from the experiment with $\Delta x \approx 3.3$ km, it is clear that the frequency of co-occurrence of GWs and enhanced shear increases with finer horizontal resolution (Fig. 15c). Although the convection is permitted in higher resolution domain, the co-relation between these two quantities exhibit the identical pattern during potential turbulent episodes (see red colors). That is to say, although the GWs are resolved with finer resolution, surprisingly, the results are not strongly dependent on the convection schema used. Nonetheless, the positive relation is evident across all simulations. As anticipated, this behaviour is consistent with the results presented in Sect. 5.1 and aligns with findings from idealized studies demonstrating that GW-induced perturbations plays a role in enhancement of shear, and thereby preconditioning the flow for shear-driven instabilities and subsequent potential turbulence generation.

To this point, the results obtained from the analysis of vertical shear and absolute GW momentum flux give potential for turbulence occurrence. In particular, it could be possible that the identified shear and small-scale structures are primarily associated with the synoptic-scale flow rather than directly linked to (clear-air) turbulence. While the preceding interpretation relies on the previous studies, this issue can be addressed more directly by examining the relationship between CAT indices and AMF.

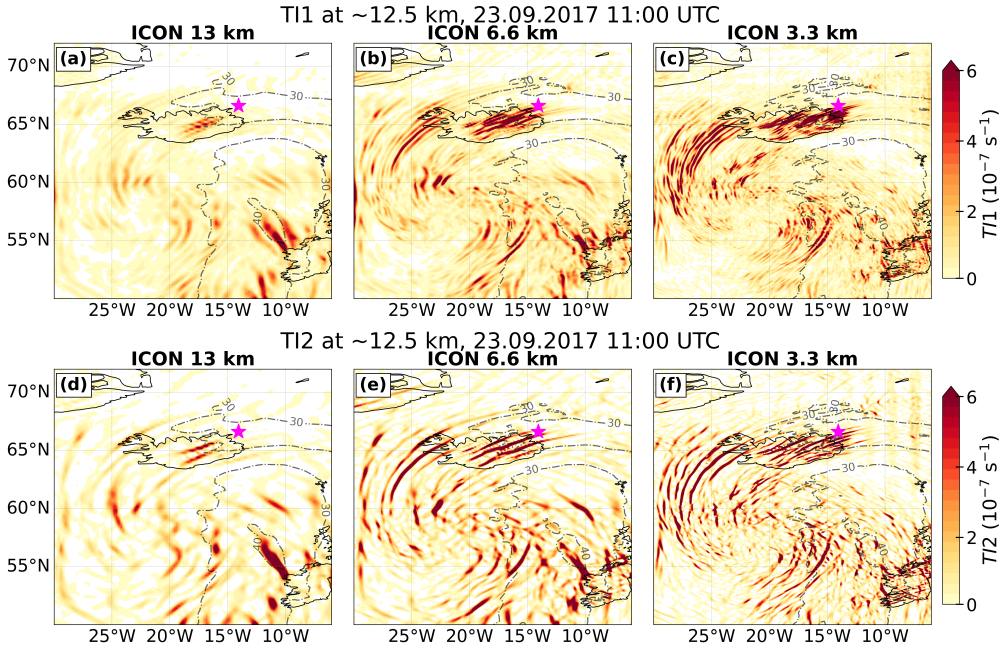


Figure 16. Distribution of turbulence indices TI1 (a-c) and TI2 (d-f) at ~12.5 km altitude for ICON 13 km, 6.5 km and 3.3 km resolution nested simulations. The dashed line represent corresponding horizontal wind speed for values greater than 30 ms^{-1}.

Again, we turn to a brief discussion on the turbulence indices TI1 and TI2 calculated on the three ICON domains to assess potential differences between the ICON domains and between ICON and ERA5. For both TI1 and TI2, there are significant changes from the coarse to the fine resolution ICON simulations. While the patterns of TI1 and TI2 emerge in the same locations, the strength and mesoscale structures vary. Banded structures of enhanced TI1 and TI2 emerge over the North Atlantic and over Iceland. These bands carry higher values for the turbulence indices as the resolution becomes finer and become more apparent in the higher resolved domain. (Fig. 16). That is to say, the higher resolution ICON simulations with nesting revealed that localized volumes of enhanced resolved and subgrid, small–scale turbulence formed in the bands of high TI1 and TI2. The more resolved small-scale structures, i.e., the appearance of such patches are more confined in space and could be attributed to a observed correlation between the AMF (i.e., the zonal wind and vertical velocity perturbations (u', w')) and small-scale shear during turbulent episodes discussed above. This is somewhat expected and is also reflected in the relative occurrence frequency of TI1 and TI2 (Fig. 17). The largest TI1 and TI2 values occur in the ICON domain with highest resolution, indicating that potential for more CAT is resolved in this domain. The question remain, whether there is also a stronger relation of these turbulence indices to the AMF.

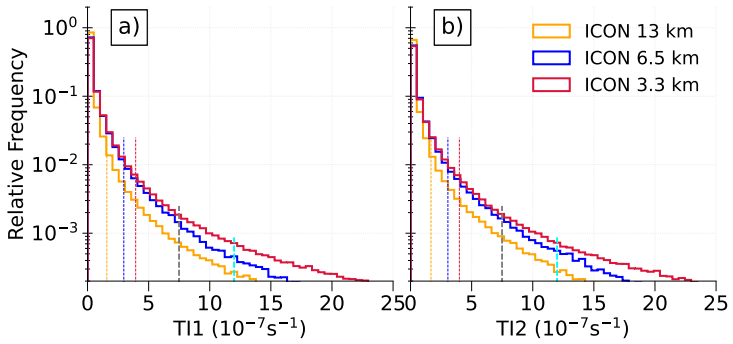


Figure 17. Relative occurrence frequency distribution of (a) TI1 and (b) TI2 for three ICON domains in the LMS. Corresponding to histogram, colored dashed lines indicate threshold retrieved as the 95th percentile over the LMS domain distribution that is considered as threshold for light moderate category. Grey and aqua lines represent the threshold for moderate ($7.5–12 \times 10^{-7}\,\mathrm{s}^{-1}$) and moderate to greater ($>12 \times 10^{-7}\,\mathrm{s}^{-1}$) intensity CAT, respectively.

From Fig. 17, it is observed that the occurrence frequency of moderate to greater intensity CAT increases with finer spatiotemporal resolution (see also Appendix C). This is also evident in the joint histograms of TI1 – AMF and TI2 – AMF pairs in the LMS domain with the stronger positive correlation between turbulence indices and AMF (Fig. 18), also across sensitivity experiments. One possible explanation for this could be the strong GW activity that is originated from the convective source in higher resolution experiments, being responsible for the amplification of shear, highlighting the fact that vertically propagating GWs, and mainly GW-induced shear, could play a significant role not only in the generation of CAT, but also in its dynamics and evolution. This suggests that improved representation of GW-like small-scale structures at higher resolution could give more accurate prediction of such turbulence events.

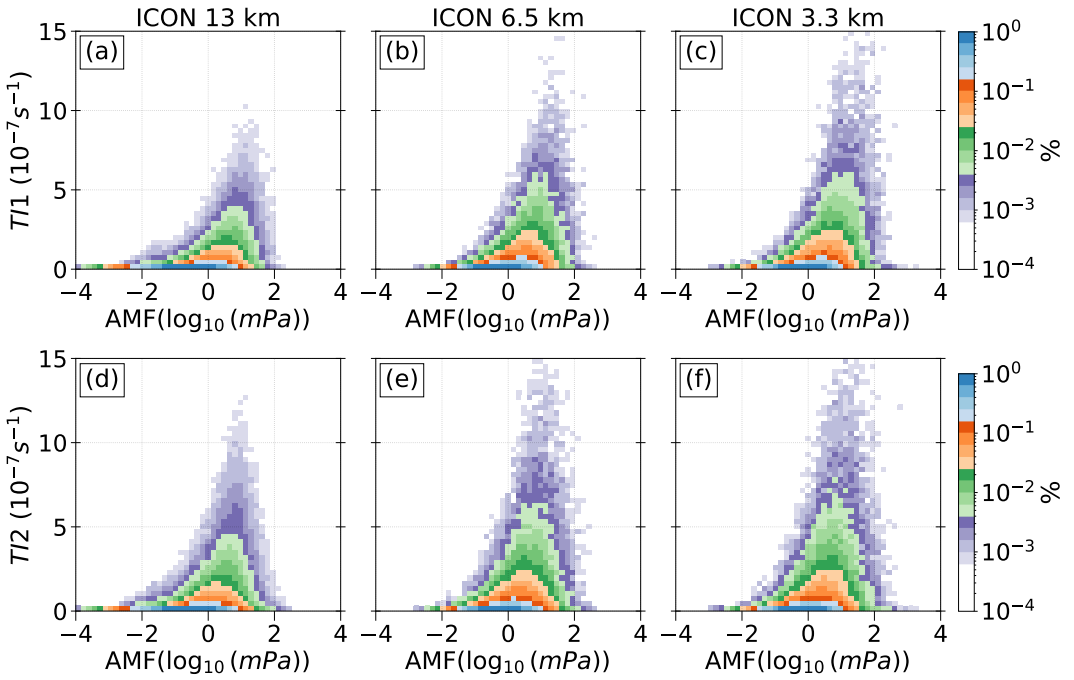


Figure 18. Frequency (%) distribution of absolute momentum flux–turbulent indices TI1 (a-c), TI2 (d-f) in pairs over the LMS for ICON 13 km, 6.5 km and 3.3 km resolution nested simulations at 11:00 UTC. Normalized counts of PDFs distribution is shown. Logarithmic occurrence frequency color scale is applied.

On the other side, the higher positive occurrences of TI1 – AMF and TI2 – AMF observed in ICON contrasts with Fig. 15, where ICON exhibits weaker and patchier shear perturbations compared to ERA5 (Fig. 7) and IFS (Fig. 11) in the vicinity of low *Ri*. A plausible explanation is that, in ICON, enhanced local flow deformation during turbulent events in the LMS partly compensates for weaker resolved shear, but leading to a higher occurrence of TI1 in regions influenced by GWs. Nonetheless, the forecast skill of DEF as a turbulence diagnostic has previously been linked to frontogenesis, enhancement of thermal wind shear (Ellrod and Knapp, 1992), and local GW activity (Kunkel et al., 2014).

Furthermore, results gain from IFS and ICON support the hypothesis that differences in spatio-temporal resolution sensitivity mainly stem from horizontally propagating GWs with large horizontal wavelengths, which dominate the horizontal derivatives of momentum fluxes. At the same time, upward-propagating large-amplitude GWs contribute predominantly to the vertical derivatives of the wind components. Ultimately, this leads to pronounced shear, lower Richardson numbers, i.e., more regions prone to becoming dynamically unstable, and higher occurrences of TI1/TI2 indices.

Combining the information obtained from the analysis based on datasets that uses hydrostatic and non-hydrostatic dynamical core, the outcomes from this analysis suggest that the representation of small-scale GWs and the computation of turbulence related fields such as TI1, TI2 are quite sensitive to the spatial and temporal resolution, to the existence of high resolution data (such as the ICON 3.3 km and 6.5 km data available for this study), as well as to the physical process considered therein.

6 Turbulence diagnostics in a zonal framework

In this section, we turn our perspective to a more general feature of the LMS which has been described recently in Kaluza et al. (2021, 2022). We first examine the occurrence of extratropical TSL (Kaluza et al., 2021) across three available datasets: two ECMWF products and a large domain ICON simulation. Afterwards, we investigate the role of GWs in the formation of the TSL and whether turbulence occurs in the region of the TSL. Note here that, we consider ICON simulation with $\Delta x \approx 13$ km, as this is the resolution closer to the ECMWF reanalysis and forecast data. This will allows us to gain a comprehensive view of synoptic-scale structures across the entire extratropical lowermost stratosphere. We first start with the shear abundance in the extratropics. The TSL has been defined via an exceedance of a defined threshold value of vertical wind shear, i.e., $S^2 \geq S_t^2$ where $S_t^2 = 4 \times 10^{-4} s^{-2}$ (Kaluza et al., 2021). We apply an analogous method to our case study at an instantaneous time step in our limited area over the North Atlantic at which we observed the GW-induced shear enhancement.

Figure 19a-c shows the relative occurrence frequencies counted in zonal direction for S^2 exceeding the threshold, i.e., $S^2 \geq S_t^2$. The datasets represents both upper tropospheric as well as lower stratospheric occurrence frequency distribution of strong shear. The above average dynamical tropopause altitude for profiles with $S^2 \geq S_t^2$ are indicative of the modulation of the tropopause by baroclinic wave ridges and the associated GW activity (see Sect. 4.1). The pronounced shear occurrences are observed in between 45° N and 60° N in ERA5 and IFS, and with slightly less abundance in ICON. This further supports the results observed in Sect. 4.2 and Sect. 5, where the LMS exhibit the high abundance of shear as well as GW momentum flux in the vicinity of potential turbulence.

We further explore this relation through the zonal occurrence of CAT indices, that means for TI1 and TI2 exceeding the threshold ($\geq 7.5 \times 10^{-7} s^{-1}$), correspond to moderate category CAT occurrences (Fig.19d-i). In the zonally integrated view of TI1, we observed the substantial TI1 occurrences at and farther northward to the highly sheared regions (Fig.19d-f). In ERA5, enhanced frequencies indicate an abundance of moderate level CAT out of total potential CAT occurrences, see the region around 50° N in the LMS. IFS rather shows the pronounced CAT between 45° N and 60° N (Fig. 19e), with wider spread out in TI2 occurrences (Fig. 19h). In contrast to the similarities noted between ICON and IFS in Sect. 5, here ICON exhibits slightly lower occurrences of CAT indices which are rather weaker but broadly distributed in TI2 (Fig. 19f, i). Overall, both TI1 and TI2 exhibit identical pattern in terms of occurrences in the LMS (compare Fig. 19d-f and g-i). Besides this, regions with enhanced shear but absent TI1 occurrences (e.g., near 35° N and 70° N in ERA5 and IFS) point to shear generated by large–scale features such as the jet stream, rather than by GWs. In sum, the turbulence diagnostics reveal turbulence hotspots near typical aircraft cruising altitudes (∼10–13.5 km) in the North Atlantic across all datasets, consistent with the altitude range where strong shear layers frequently occur.

The question remains whether the GWs are of any relevance to the extratropical TSL and now to the CAT hotspots. The shorter GWs that propagate more vertically carry a greater absolute momentum flux. One would expect momentum-flux deposition in the region where GW-induced turbulence and CAT occur. In this case, the largest magnitudes of AMF appear to be concentrated in the upper troposphere that extend upward into the lower stratosphere (see Fig. D1). On first glance, the AMF exhibits high magnitudes and sharp gradients in the vertical in regions of strong shear $S^2 \geq S_t^2$ and potential turbulence in the LMS. However,

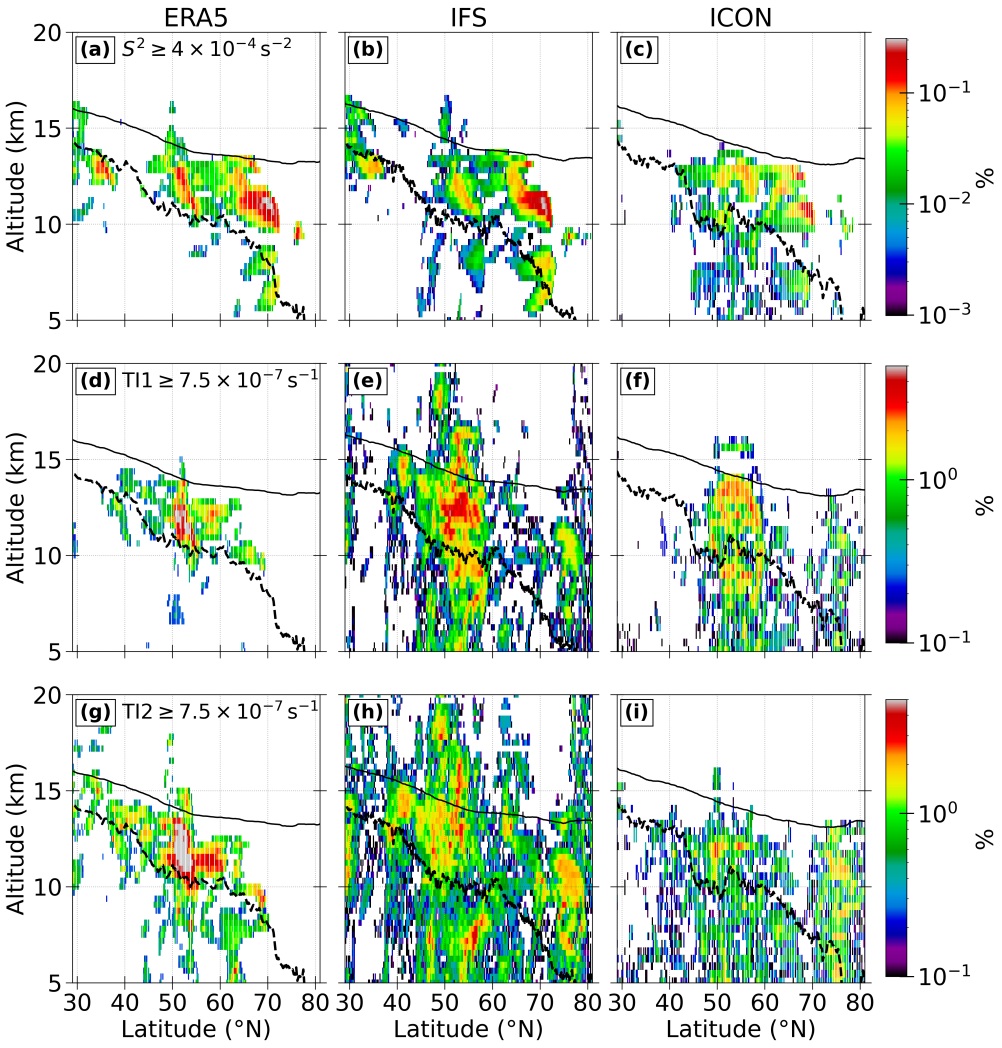


Figure 19. Relative occurrence frequency distribution of grid volumes that exhibit (a-c) $S^2 \geq 4 \times 10^{-4} s^{-2}$, (d-f) TI1 $\geq 7.5 \times 10^{-7} s^{-1}$ and (g-i) TI2 $\geq 7.5 \times 10^{-7} s^{-1}$ over the North Atlantic domain on 23rd September 2017, 11:00 UTC for ERA5, IFS, and ICON. Panels (d–i) represent regions of moderate-intensity CAT occurrence. The occurrence frequencies are shown with logarithmic frequency contours, displaying the data in bins of sizes $\Delta y = 0.2°$ and $\Delta z = 500\,\text{m}$. The zonal-mean dynamical tropopause (3.5 PVU isosurface; black dashed line) and the zonal-mean 380 K isentrope of potential temperature (solid line) are overlaid.

if GWs plays a role, we could expect at least quasi-spatial co-occurrence of above observed enhanced shear and high intensity turbulent indices with GW momentum flux.

665 Figure 20 represents AMF in the shear-dominated regions as well in the moderate intensity CAT prone region. The AMF in the vicinity of strong shear highlights predominantly enhanced flux above the tropopause in ERA5 and IFS, particularly in the midlatitude belt (Fig. 20a, b). It is worth noting that, ERA5 exhibits a pattern akin to IFS, albeit with less spatial resolution.

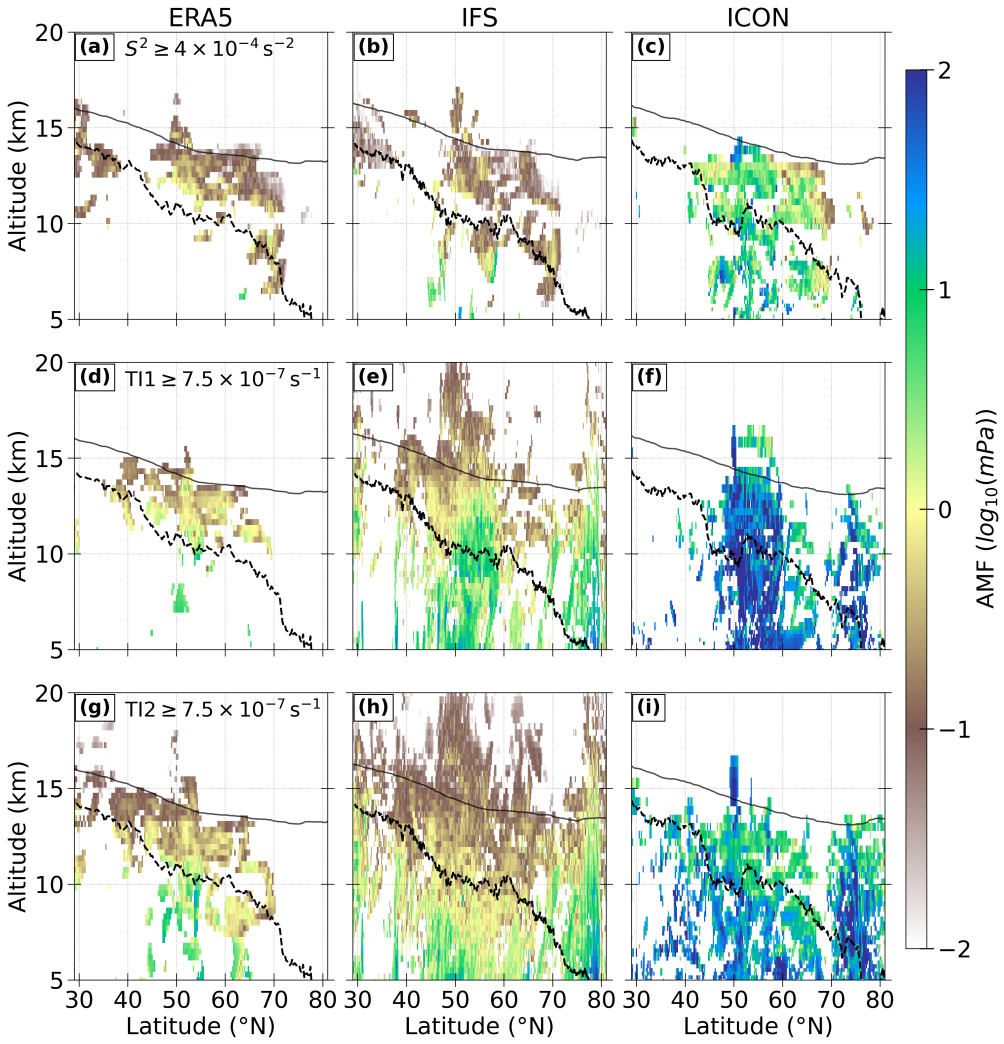


Figure 20. Zonal mean resolved GW absolute momentum flux (AMF, $log_{10}(mPa)$) values conditioned on regions where (a-c) $S^2 \geq S_t^2$, (d-f) TI1 $\geq 7.5 \times 10^{-7} s^{-1}$ and (g-i) TI2 $\geq 7.5 \times 10^{-7} s^{-1}$. All values are vertically binned with $\Delta z = 500$ m. The zonal-mean dynamical tropopause (3.5 PVU isosurface; black dashed line) and the zonal-mean 380 K isentrope of potential temperature (solid line) are overlaid.

Meanwhile ICON exhibits more localized but more intense AMF in the vicinity of strong shear (Fig. 20c). The observed fluxes suggest strong GWs activity associated with baroclinic disturbances. Interestingly, the areas of pronounced shear are mostly also the regions of highly amplified GW activity. This overlap confirms the aforementioned relationship between GWs and enhanced shear and gives the plausibility of the significant contribution of small–scales to turbulent mixing. This findings further agree with the conclusion of the previous studies of baroclinic life cycles (Kaluza et al., 2019, 2021) and process study (Kunkel et al., 2019; Umbarkar and Kunkel, 2025).

Finally, the relation between GWs and CAT is assessed by the AMF in the vicinity of TI1 (Fig. 20d-f) and TI2 (Fig. 20g-i). In ERA5, turbulence hotspots coincide with strong GW activity, with GW fluxes dominating across the tropopause and at the LMS. Next, IFS exhibits broader AMF spectrum characterized by strong vertical gradient in the vicinity of higher TI1 and a wider spatial extent in TI2 (Fig. 20e, h). In contrast, ICON exhibits more intense small–scale flux structures and vertical gradients throughout the UTLS, could be associated with resolved GWs (Fig. 20f, i). In principle, there are observed higher vertical gradients of AMF where we have enhanced (clear-air) turbulence. This distinction underlines the specific contribution of GWs to the observed turbulence hotspots.

Besides this, some uncertainty remains in the quantitative assessment of GW momentum fluxes, as the representation of unresolved sources may affect both their magnitude and distribution. An important note is that ICON has been shown to reproduce satellite-derived GW flux patterns without requiring additional parameterizations for unresolved waves over the middle stratosphere (Stephan et al., 2019b). However, Toghraei et al. (2025) suggests that its non-orographic parameterizations may underestimate the dynamical filtering of westward-propagating waves in the mid-latitude region. Nonetheless, the enhanced wave momentum fluxes co-located with regions of high TI1 occurrence, supports the link between GW activity and CAT generation in the UTLS.

Overall, these findings support the hypothesis that subgrid or small–scale GWs contribute substantially to the enhanced shear formation, the development of high intensity CAT, and hence, consequently could contribute to shaping the ExTL dynamics.

7 Discussion and conclusion

The present study highlights the role of gravity wave induced shear as a key parameter for the tropopause shear layer (TSL, Kaluza et al., 2021) on the basis of observations, reanalysis and forecast data. We note that this is key for the potential occurrence of clear air turbulence, which manifests as highly transient yet frequent mixing processes in the extratropical lowermost stratosphere. As such these processes may play a crucial role in the formation and maintenance of extratropical transition layer, alongside other processes such as convective injection.

Based on idealized studies of the GW-scale cascade process in Umbarkar and Kunkel (2025), we here examine this relation in depth in a more realistic environment, for the atmospheric state over the North Atlantic during an episode of the airborne mission WISE. On the one side we use airborne measurements and additionally a comprehensive model forecast dedicated for this case with ICON. In addition to ERA5 reanalysis data and IFS forecast data, the latter allows us to study this case also in a comprehensive ICON model forecast which has been dedicated for this case study. Specifically, we use time series analysis, trace species profiles, tracer-tracer correlations and spectral analysis along with a recently explored hybrid approach based on Helmholtz decomposition method (Wei et al., 2022), to better understand the relation between gravity waves, vertical wind shear and turbulence occurrence in the lowermost stratosphere. In summary, we come to the following results:

- **Observations** from airborne measurements show mixed air masses in the vicinity of GW activity and vertical shear occurrence. We analyzed a flight of the WISE campaign over the North Atlantic, where tracer-tracer correlations of CO and N_2O revealed the occurrence of mixed air masses. Vertical profiles of these trace gases indicated that these mixed

air masses resided in the LMS between 345 K and 375 K. Further analysis revealed that the mixing might be in relation to GWs and that the mixing occurred very recently in regions of persistently low Richardson numbers and enhanced vertical wind shear.

- The synoptic situation based on ERA5 reveals persistent GW activity over the Icelandic highlands that has their source of origin from flow over orography. ERA5, despite its coarser horizontal resolution, captures upward propagating large-amplitude GWs, which further affect the vertical gradients of the wind components that lead to shear generation.

- The potential role of GWs in the generation of shear and turbulence in the LMS is identified through a spatio-temporal co-occurrences of small-scale momentum flux, enhanced shear, and low Richardson numbers. GW-induced enhanced shear, which are conducive to turbulence, highly correlates with appearance of envelopes (or packets) of small–scale GWs of $\sim$100 km of wavelength in the LMS with the same characteristics. Spectral function detects downscale energy transfer from small-scale GWs that intensifies shear near $\sim$340 K, thereby creating conditions conducive to the generation of (clear-air) turbulence. Further analysis of turbulence diagnostics including Ri on large-scale and turbulence indices (TI1, TI2) on small-scale suggests that GWs produce shear which leads to the potential occurrence of clear air turbulence.

- The dynamical situation is very similarly represented in ECMWF ERA5 and IFS forecast data. As expected the finer resolved forecast data shows more features on the mesoscale. In turn, the enhanced vertical shear occurs less frequent in ERA5 compared to the IFS. Nonetheless, ERA5 does capture a large portion of GW spectrum and most of the enhanced shear encounters. As such the reanalysis data provides valuable information on the spectral characteristics of GWs and is therefore suitable for long term analysis of GW-induced shear, at least over the North Atlantic. In this context, different levels of information can be targeted: ERA5 is well suited to characterize the large-scale environment and regions favourable for GW activity, and to some extent their resolved spectral characteristics, whereas its limited effective resolution constrains its ability to accurately represent small-scale shear and turbulence.

- The high-resolution ICON simulations reproduced a large-amplitude GW event on 23^{rd} September 2017 over the North Atlantic reasonably well. Application of vertical momentum fluxes and shear perturbations analysis, flow instability as well as turbulent metrics point to multiscale interactions dominated by upward-propagating large-amplitude GWs with relatively short horizontal but large vertical wavelengths.

- Further analysis of comprehensive ICON model forecast reveal that the GW appearance and associated vertical shear are strongly depend on the model grid spacing. Although GW activity in the tropopause region is enhanced in case of the convection-permitted simulations, the relation of GW with shear and turbulence remains relatively constant in the convection-parametrized experiments. Compared to the ECMWF models, ICON exhibits slightly lower shear occurrences, raising a question of whether resolving smaller-scale GWs redistributes variance and reduces diagnosed shear or whether there are other source for this discrepancies related the model formulation or setup.

- While larger differences are apparent in GWs and shear between ECMWF model products and ICON, this is not as pronounced anymore for turbulence indices. The diagnosed turbulent regions display strongly banded structures asso-

ciated with GWs and GW-induced shear, parallel to the upper-level front, that is closely linked to baroclinic activity and associated tropopause variability (Kaluza et al., 2021). ERA5 and IFS indicate widespread potential for the occurrence of dynamic instability, while ICON shows weaker shear perturbations but higher AMF at low Ri. Regarding CAT indices, ERA5 shows signatures of moderate intensity CAT in the LMS associated with strong GW activity, with IFS and ICON mimic this pattern but with slightly higher intensity of CAT. In sum, this highlights the substantial role of GWs in enhancing shear and fostering high-intensity CAT in the LMS, with ERA5 capturing both GW spectra and their contribution to shear and turbulence, making it suitable for long-term studies over the North Atlantic.

The relation between small–scale GW momentum flux has long been used as a reliable index for GW analysis (Plougonven et al., 2003, 2017; Lachnitt et al., 2023; Umbarkar and Kunkel, 2025), hinting towards the possibility for the active role of GWs in producing shear hotspots along with irreversible mixing of air masses in the lowermost stratosphere. However, further research should address the seasonal and geographical variability of small–scale, GW–induced shear over the mid-latitude region.

The similarities and differences we find here are certainly model, resolution and parameterization dependent. While ICON demonstrates skill in reproducing GW flux patterns comparable to those in IFS, questions remain as to whether resolved GW amplitudes in the extratropics are fully converged across resolutions, and how parameterized sources interact with the resolved spectrum. To a certain extent, this is supported by the fact that high-resolution simulations have not yet converged when it comes to GWs in the extratropics (Kruse et al., 2022; Polichtchouk et al., 2023; Gupta et al., 2024).

In summary, the resulting picture presented by a synthesis of our findings in one cascade of processes across scales: starting with inertia GWs associated with the flow over orography, proceeding through the generation of enhanced shear mechanism, with excitation of shear instabilities at the small scales where potential turbulence was generated and ending with the energy-momentum transfer in the vertical. In conclusion, our analysis highlights GW-induced shear as a driver of UTLS transport and mixing, as well as a source of CAT occurrences, meriting further investigation into its prevalence in the geographic location and its potential implications for both climate processes, particularly the redistribution of H_2O and O_3 and their associated radiative forcing (e.g., Riese et al., 2012), and aviation forecasting (e.g. Kim and Chun, 2011; Sharman and Pearson, 2017). Overall, the GW related processes should be considered as the important candidate for the interpretation of CAT in the extratropical UTLS.

Data availability. The WISE flight data is available on the HALO-DB. The data used for this paper is available on Zenodo (Umbarkar, 2025) (last access: 08 September 2025). ERA5 model level data was retrieved from the MARS archive. The data is also publicly available from Copernicus Climate Change Service (C3S) Climate Data Store using the CDS API. The dataset used is: "ERA5: Fifth generation of ECMWF atmospheric reanalyses of the global climate" https://doi.org/10.24381/cds.143582cf (last access: 08 September 2025). IFS forecast data was retrieved from the MARS archive. The ICON source code is distributed under an institutional license issued by the German Weather Service (DWD). The ICON model output used in this study is available upon reasonable request .

Appendix A: Supporting figures to selected methodology, synoptic situation and hodograph analysis

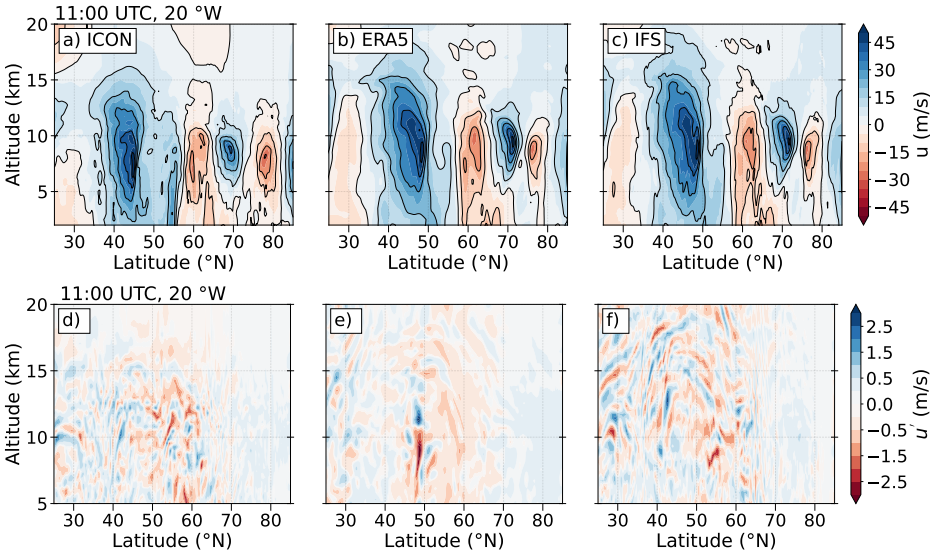


Figure A1. Vertical cross section of zonal wind u (upper panel) and retrieved u perturbations (lower panel) on 23 September 2017 11:00 UTC at 20°W for (a, d) ICON, (b, e) ERA5, and (c, f) IFS.

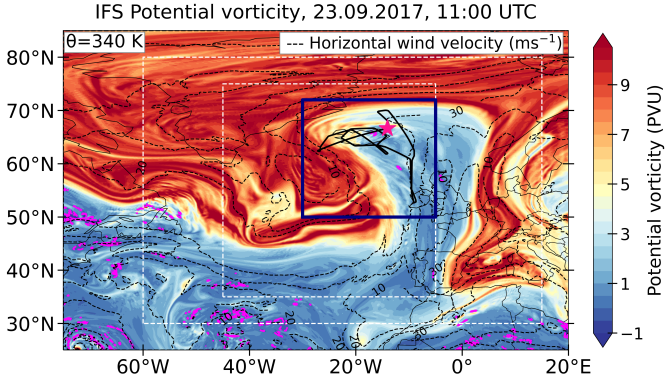


Figure A2. IFS potential vorticity distribution (in PVU) at the 340 K isentropic surface on 23.09.2017 at 11:00 UTC. The dashed lines show the horizontal wind (in m s^{-1}) on 340 K. The thick black line shows the flight path of RF05 and the star marks the aircraft position at 11:00 UTC. Magenta color shows the negative PV values.

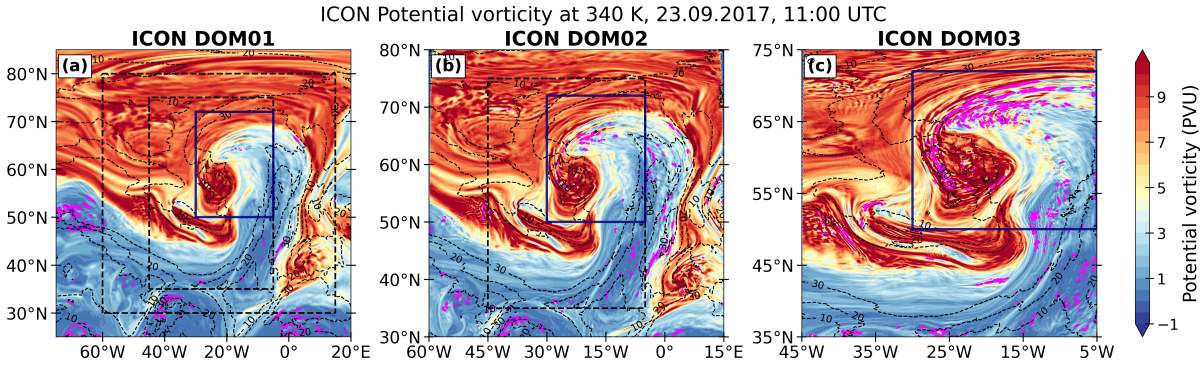


Figure A3. Potential vorticity distribution (in PVU) at the 340 K isentropic surface on 23.09.2017 at 11:00 UTC for three ICON domains: (a) ICON 13 km (b) ICON 6.5 km and (c) ICON 3.3 km. The dashed lines show the horizontal wind (in m s^{-1}) on 340 K. Magenta color shows the negative PV values, while blue box represent analysis domain selected for this study.

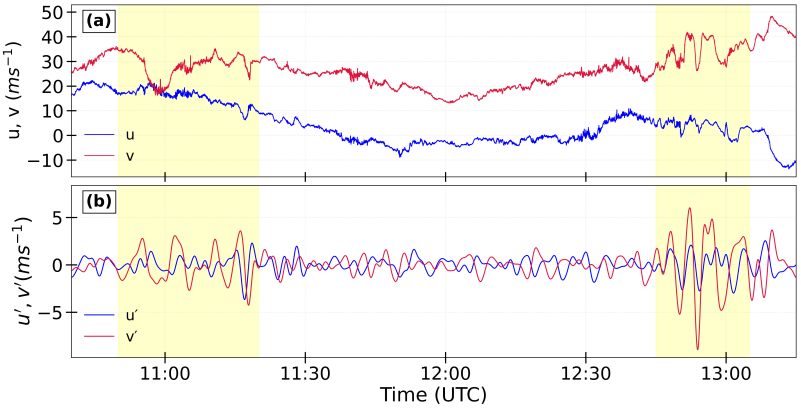


Figure A4. Time series of (a) zonal (u, ms^{-1}; blue) and meridional (v, ms^{-1}; red) wind component from HALO for WISE RF05, the shaded yellow regions same as Fig. 3, whereas panel (b) shows perturbation of u and v obtained from Butterworth filter.

Appendix B: Supporting information to the GW and shear analysis

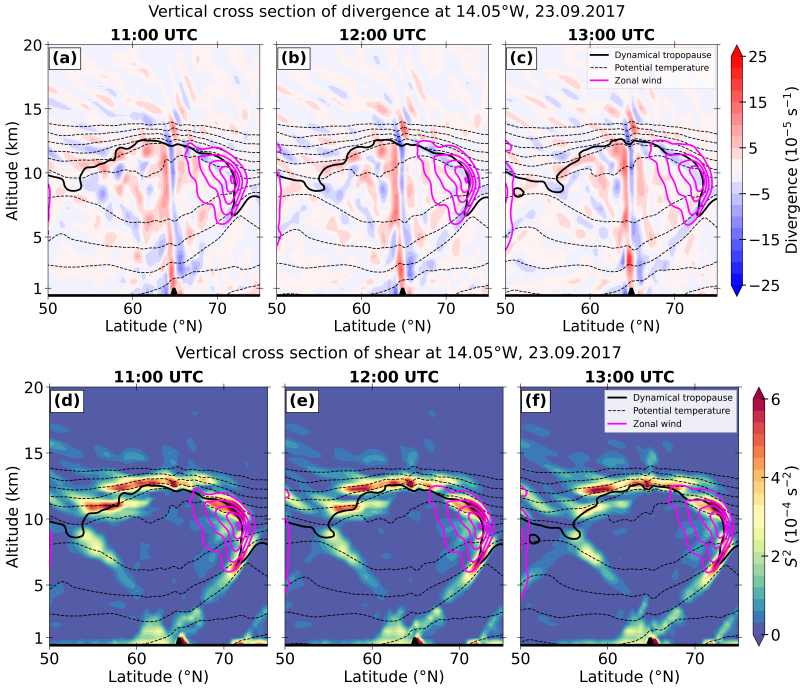


Figure B1. Vertical cross sections of divergence (a-c) and vertical shear (d-f) at longitude 14.05° W for ERA5 data at 11:00 UTC,12:00 UTC and 13:00 UTC. The solid black line represent the 3.5 PVU as a dynamical tropopause whereas dashed lines in lower panel represent the potential temperature starting from 280 K (bottom) to 380 K (top) with 10 K increments.

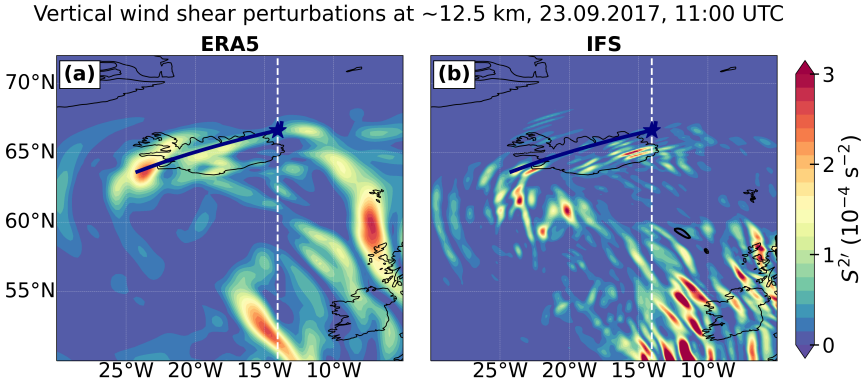


Figure B2. Distribution of vertical wind shear perturbations $S^{2'}$ at 12.5 km altitude for (a) ERA5 and (b) IFS.

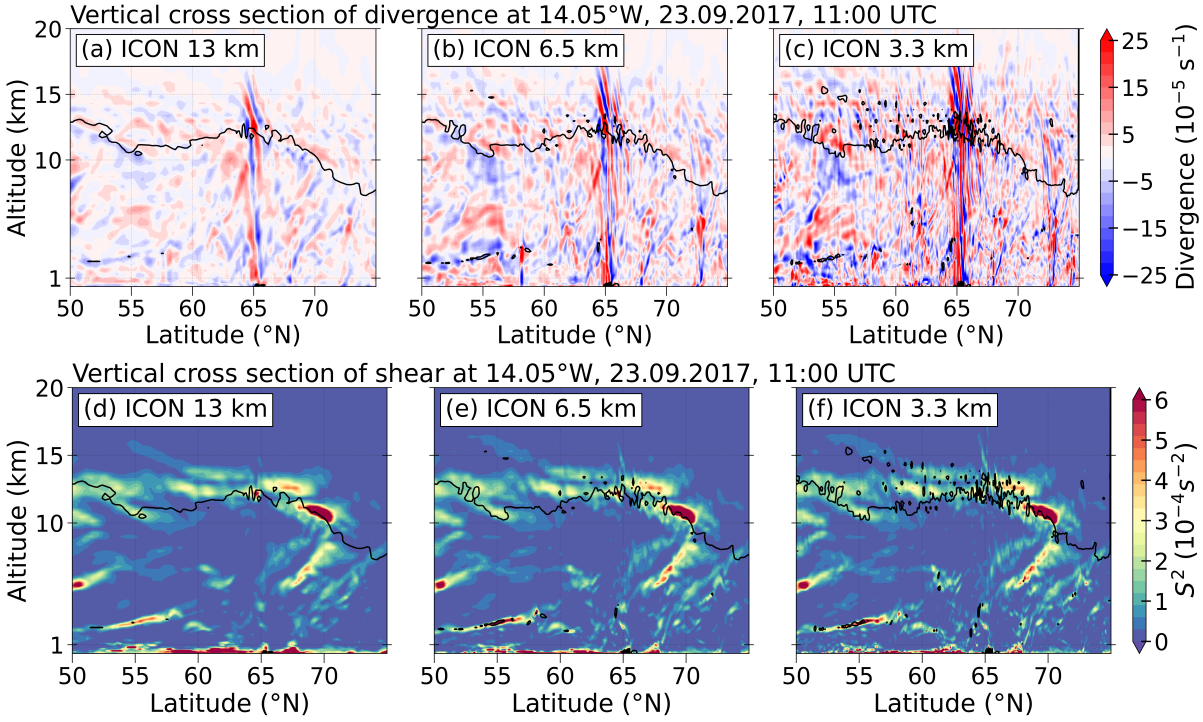


Figure B3. Vertical cross sections of divergence (a-c) and vertical shear (d-f) at longitude 14.05° W for three ICON domains. The solid black line represent the 3.5 PVU as a dynamical tropopause.

Appendix C: Supporting information to the CAT analysis

We use all data points in the LMS i.e., between 3.5 PVU and 380 K, to derive PDF distribution of the small–scale TI1 and TI2 indices. We then calculate the 95th percentile values of these distributions, which are used as threshold values. The resulting TI1 threshold values for ERA5, IFS and ICON are $1.4 \times 10^{-7} s^{-1}$, $2.1 \times 10^{-7} s^{-1}$ and $1.5 \times 10^{-7} s^{-1}$ respectively. There are only minor difference in the threshold observed across the datasets. Given the range of values in PDFs and the differences in the underlying data, the gained thresholds differ only slightly across the datasets, with some differing up to a factor of two. Furthermore, the more GW related index TI2, gained from the inclusion of convergent flow, applies the same threshold criterion as TI1, where the resulting thresholds are $1.5 \times 10^{-7} s^{-1}$, $2.45 \times 10^{-7} s^{-1}$, and $1.5 \times 10^{-7} s^{-1}$ for ERA5, IFS and ICON, respectively. We categorize the CAT levels based on the thresholds: light to moderate from respective 95th percentile threshold, moderate ($7.5 \times 10^{-7} s^{-1}$ to $12 \times 10^{-7} s^{-1}$), and moderate-or-greater ($>12 \times 10^{-7} s^{-1}$), consistent with previous studies (e.g., Ellrod and Knapp, 1992; Thompson and Schultz, 2021).

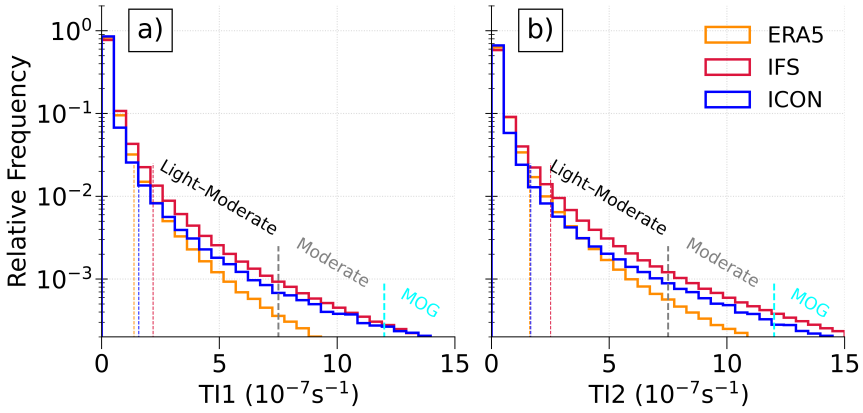


Figure C1. Relative occurrence frequency distribution of (a) TI1 and (b) TI2 for ERA5, IFS and ICON in the LMS domain. Corresponding to histogram, colored dashed lines indicate threshold retrieved as the 95th percentile over the LMS domain that is considered as threshold for light moderate category. Grey and aqua lines represent the threshold for moderate (7.5-$12 \times 10^{-7} s^{-1}$) and moderate to greater (moderate to greater; $> 12 \times 10^{-7} s^{-1}$) intensity clear air turbulence, respectively.

ICON sensitivity: CAT threshold selection

The relative occurrence frequency distribution of TI1 and TI2 for three ICON nested domains in the LMS is shown in Fig. 17. The threshold criterion is based on 95th percentile for each case in the LMS and is same as in ERA5. Based on this, the resulting TI1 threshold values for simulations with $\Delta x \approx 13$ km, $\Delta x \approx 6.5$ km, and $\Delta x \approx 3.3$ km are $1.5 \times 10^{-7}\,\mathrm{s}^{-1}$, $3.21 \times 10^{-7}\,\mathrm{s}^{-1}$, and $4.03 \times 10^{-7}\,\mathrm{s}^{-1}$, respectively; and for TI2, the resultant threshold values are $1.72 \times 10^{-7}\,\mathrm{s}^{-1}$, $3.75 \times 10^{-7}\,\mathrm{s}^{-1}$, and $4.31 \times 10^{-7}\,\mathrm{s}^{-1}$, respectively. For the comparison across experiments and following the previous studies (e.g., Thompson and Schultz, 2021), the threshold values are kept common for moderate (7.5–$12 \times 10^{-7}\,\mathrm{s}^{-1}$) and moderate to greater ($>12 \times 10^{-7}\,\mathrm{s}^{-1}$) categories.

Appendix D: Supporting information to "Turbulence diagnostics in a zonal framework"

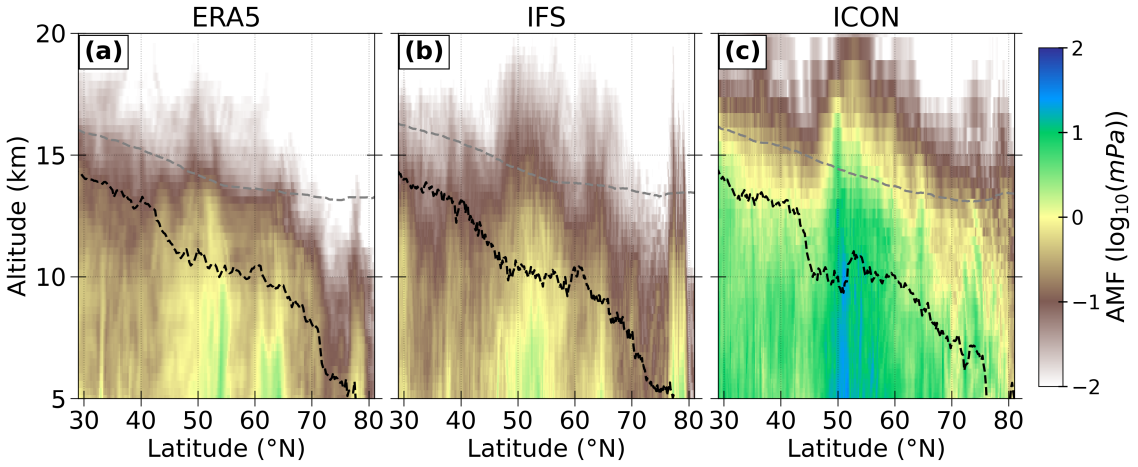


Figure D1. Zonal mean GW absolute momentum flux (AMF, $log_{10}(mPa)$) for (a) ERA5, (b) IFS and (c) ICON ≈13 km.

Author contributions. MU and DK conceptualized the core research questions and goals. CS and AM set up and conducted the ICON simulations. TK, HCL, and PH provided the WISE campaign data. MU performed the data analysis, post-processing, and prepared the initial draft of the manuscript. MU and DK jointly revised and edited the manuscript. All authors contributed to and commented on the manuscript.

Competing interests. The authors have no conflict of interest.

Acknowledgements. This work was funded by the Deutsche Forschungsgemeinschaft (DFG, German Research Foundation) – TRR 301 – Project-ID 428312742: “The tropopause region in a changing atmosphere, https://tpchange.de" (last access: 08 September 2025) sub-project B06. WISE campaign was supported by the German Science Foundation (DFG) within the priority program HALO SPP 1294, (KU 3524/1-1, HO 4225/7-1, and HO 4225/8-1). We gratefully acknowledge the computing time provided on the supercomputer MOGON II at Johannes Gutenberg University Mainz (https://hpc.uni-mainz.de) (last access: 08 September 2025). We further thank Ulrich Achatz and Juerg Schmidli from Goethe-Universität Frankfurt for their valuable comments and feedback on this work.

References

Achatz, U., Alexander, M. J., Becker, E., Chun, H. Y., Dörnbrack, A., Holt, L., Plougonven, R., Polichtchouk, I., Sato, K., Sheshadri, A., Stephan, C. C., Van Niekerk, A., and Wright, C. J.: Atmospheric Gravity Waves: Processes and Parameterization, Journal of the Atmospheric Sciences, 81, 237–262, https://doi.org/10.1175/JAS-D-23-0210.1, 2024.

Alexander, M. J. and Grimsdell, A. W.: Seasonal cycle of orographic gravity wave occurrence above small islands in the Southern Hemisphere: Implications for effects on the general circulation, Journal of Geophysical Research: Atmospheres, 118, https://doi.org/10.1002/2013jd020526, 2013.

Alexander, M. J., Geller, M., McLandress, C., Polavarapu, S., Preusse, P., Sassi, F., Sato, K., Eckermann, S., Ern, M., Hertzog, A., Kawatani, Y., Pulido, M., Shaw, T. A., Sigmond, M., Vincent, R., and Watanabe, S.: Recent developments in gravity-wave effects in climatemodels and the global distribution of gravity-wavemomentum flux from observations and models, Quarterly Journal of the Royal Meteorological Society, 136, 1103–1124, https://doi.org/10.1002/qj.637, 2010.

Appenzeller, C., Holton, J. R., and Rosenlof, K. H.: Seasonal variation of mass transport across the tropopause, Journal of Geophysical Research: Atmospheres, 101, 15 071–15 078, https://doi.org/10.1029/96jd00821, 1996.

Berthet, G., Esler, J. G., and Haynes, P. H.: A Lagrangian perspective of the tropopause and the ventilation of the lowermost stratosphere, Journal of Geophysical Research: Atmospheres, 112, https://doi.org/10.1029/2006jd008295, 2007.

Birner, T.: Fine-scale structure of the extratropical tropopause region, Journal of Geophysical Research Atmospheres, 111, 1–14, https://doi.org/10.1029/2005JD006301, 2006.

Birner, T., Dörnbrack, A., and Schumann, U.: How sharp is the tropopause at midlatitudes?, Geophysical Research Letters, 29, 1–4, https://doi.org/10.1029/2002GL015142, 2002.

Butterworth, S.: On the theory of filter amplifiers, Experimental wireless and the wireless engineer, 7, 536–541, 1930.

Dörnbrack, A.: Transient Tropopause Waves, Journal of the Atmospheric Sciences, 81, 1647–1668, https://doi.org/10.1175/jas-d-24-0037.1, 2024.

Dörnbrack, A., Bechtold, P., and Schumann, U.: High-Resolution Aircraft Observations of Turbulence and Waves in the Free Atmosphere and Comparison With Global Model Predictions, Journal of Geophysical Research: Atmospheres, 127, https://doi.org/10.1029/2022jd036654, 2022.

Dörnbrack, A., Lachnitt, H., Hoor, P., and Imazio, P. R.: Multiscale Dynamical Processes Shaping a Mixing Line, Journal of Geophysical Research: Atmospheres, 130, https://doi.org/10.1029/2025jd043527, 2025.

Durran, D. R.: Pseudomomentum Diagnostics for Two-Dimensional Stratified Compressible Flow, Journal of Atmospheric Sciences, 52, 3997 – 4009, https://doi.org/10.1175/1520-0469(1995)052<3997:PDFTDS>2.0.CO;2, 1995.

Ellrod, G. P. and Knapp, D. I.: An Objective Clear-Air Turbulence Forecasting Technique: Verification and Operational Use, Weather and Forecasting, 7, 150–165, https://doi.org/10.1175/1520-0434(1992)007<0150:aocatf>2.0.co;2, 1992.

Fritts, D. C. and Alexander, M. J.: Gravity wave dynamics and effects in the middle atmosphere, Reviews of Geophysics, 41, 1–64, https://doi.org/10.1029/2001RG000106, 2003.

Geller, M. A., Alexander, M. J., Love, P. T., Bacmeister, J., Ern, M., Hertzog, A., Manzini, E., Preusse, P., Sato, K., Scaife, A. A., and Zhou, T.: A Comparison between Gravity Wave Momentum Fluxes in Observations and Climate Models, Journal of Climate, 26, 6383–6405, https://doi.org/10.1175/jcli-d-12-00545.1, 2013.

Gomes, M. B., Shapiro, A., Parsons, D. B., and Gebauer, J. G.: Using a Numerical Model to Evaluate a Proposed Mechanism for Nocturnal Low-Level Jets and Ascent over a Warm Tongue, Monthly Weather Review, 153, 1265–1281, https://doi.org/10.1175/mwr-d-24-0111.1, 2025.

Guest, F. M., Reeder, M. J., Marks, C. J., and Karoly, D. J.: Inertia–Gravity Waves Observed in the Lower Stratosphere over Macquarie Island, Journal of the Atmospheric Sciences, 57, 737–752, https://doi.org/10.1175/1520-0469(2000)057<0737:igwoit>2.0.co;2, 2000.

Gultepe, I., Sharman, R., Williams, P. D., Zhou, B., Ellrod, G., Minnis, P., Trier, S., Griffin, S., Yum, S. S., Gharabaghi, B., Feltz, W., Temimi, M., Pu, Z., Storer, L. N., Kneringer, P., Weston, M. J., Chuang, H.-y., Thobois, L., Dimri, A. P., Dietz, S. J., França, G. B., Almeida, M. V., and Neto, F. L. A.: A Review of High Impact Weather for Aviation Meteorology, Pure and Applied Geophysics, 176, 1869–1921, https://doi.org/10.1007/s00024-019-02168-6, 2019.

Gupta, A., Birner, T., Dörnbrack, A., and Polichtchouk, I.: Importance of Gravity Wave Forcing for Springtime Southern Polar Vortex Breakdown as Revealed by ERA5, Geophysical Research Letters, 48, https://doi.org/10.1029/2021GL092762, 2021.

Gupta, A., Sheshadri, A., Alexander, M. J., and Birner, T.: Insights on Lateral Gravity Wave Propagation in the Extratropical Stratosphere From 44 Years of ERA5 Data, Geophysical Research Letters, 51, https://doi.org/10.1029/2024gl108541, 2024.

Hegglin, M. I., Boone, C. D., Manney, G. L., and Walker, K. A.: A global view of the extratropical tropopause transition layer from Atmospheric Chemistry Experiment Fourier Transform Spectrometer O3, H2O, and CO, Journal of Geophysical Research Atmospheres, 114, 1–18, https://doi.org/10.1029/2008JD009984, 2009.

Heller, R., Voigt, C., Beaton, S., Dörnbrack, A., Giez, A., Kaufmann, S., Mallaun, C., Schlager, H., Wagner, J., Young, K., and Rapp, M.: Mountain waves modulate the water vapor distribution in the UTLS, Atmospheric Chemistry and Physics, 17, 14 853–14 869, https://doi.org/10.5194/acp-17-14853-2017, 2017.

Hersbach, H., Bell, B., Berrisford, P., Hirahara, S., Horányi, A., Muñoz-Sabater, J., Nicolas, J., Peubey, C., Radu, R., Schepers, D., Simmons, A., Soci, C., Abdalla, S., Abellan, X., Balsamo, G., Bechtold, P., Biavati, G., Bidlot, J., Bonavita, M., De Chiara, G., Dahlgren, P., Dee, D., Diamantakis, M., Dragani, R., Flemming, J., Forbes, R., Fuentes, M., Geer, A., Haimberger, L., Healy, S., Hogan, R. J., Hólm, E., Janisková, M., Keeley, S., Laloyaux, P., Lopez, P., Lupu, C., Radnoti, G., de Rosnay, P., Rozum, I., Vamborg, F., Villaume, S., and Thépaut, J.: The ERA5 global reanalysis, Quarterly Journal of the Royal Meteorological Society, 146, 1999–2049, https://doi.org/10.1002/qj.3803, 2020.

Hirota, I. and Niki, T.: Inertia-Gravity Waves in the Troposphere and Stratosphere Observed by the MU Radar, Journal of the Meteorological Society of Japan. Ser. II, 64, 995–999, https://doi.org/10.2151/jmsj1965.64.6_995, 1986.

Holt, L. A., Alexander, M. J., Coy, L., Liu, C., Molod, A., Putman, W., and Pawson, S.: An evaluation of gravity waves and gravity wave sources in the Southern Hemisphere in a 7 km global climate simulation, Quarterly Journal of the Royal Meteorological Society, 143, 2481–2495, https://doi.org/10.1002/qj.3101, 2017.

Holton, J. R., Haynes, P. H., McIntyre, M. E., Douglass, A. R., Rood, R. B., and Pfister, L.: Stratosphere-troposphere exchange, Reviews of Geophysics, 33, 403–439, https://doi.org/10.1029/95RG02097, 1995.

Hooke, W. H.: Gravity Waves, p. 272–288, American Meteorological Society, ISBN 9781935704201, https://doi.org/10.1007/978-1-935704-20-1_12, 1986.

Hoor, P., Gurk, C., Brunner, D., Hegglin, M. I., Wernli, H., and Fischer, H.: Seasonality and extent of extratropical TST derived from in-situ CO measurements during SPURT, Atmospheric Chemistry and Physics, 4, 1427–1442, https://doi.org/10.5194/acp-4-1427-2004, 2004.

Hoor, P., Wernli, H., Hegglin, M. I., and Bönisch, H.: Transport timescales and tracer properties in the extratropical UTLS, Atmospheric Chemistry and Physics, 10, 7929–7944, https://doi.org/10.5194/acp-10-7929-2010, 2010.

Jaeger, E. B. and Sprenger, M.: A Northern Hemispheric climatology of indices for clear air turbulence in the tropopause region derived from ERA40 reanalysis data, Journal of Geophysical Research Atmospheres, 112, 1–13, https://doi.org/10.1029/2006JD008189, 2007.

Jewtoukoff, V., Hertzog, A., Plougonven, R., Cámara, A. d. l., and Lott, F.: Comparison of Gravity Waves in the Southern Hemisphere Derived from Balloon Observations and the ECMWF Analyses, Journal of the Atmospheric Sciences, 72, 3449–3468, https://doi.org/10.1175/jas-d-14-0324.1, 2015.

Jovanovic, G.: Gravity waves as a mechanism of troposphere–stratosphere–mesosphere coupling during sudden stratospheric warming, Atmospheric Chemistry and Physics, 25, 2979–2988, https://doi.org/10.5194/acp-25-2979-2025, 2025.

Kaluza, T., Kunkel, D., and Hoor, P.: Composite analysis of the tropopause inversion layer in extratropical baroclinic waves, Atmospheric Chemistry and Physics, 19, 6621–6636, https://doi.org/10.5194/acp-19-6621-2019, 2019.

Kaluza, T., Kunkel, D., and Hoor, P.: On the occurrence of strong vertical wind shear in the tropopause region: a 10-year ERA5 northern hemispheric study, Weather and Climate Dynamics, 2, 631–651, https://doi.org/10.5194/wcd-2-631-2021, 2021.

Kaluza, T., Kunkel, D., and Hoor, P.: Analysis of Turbulence Reports and ERA5 Turbulence Diagnostics in a Tropopause-Based Vertical Framework, Geophysical Research Letters, 49, https://doi.org/10.1029/2022gl100036, 2022.

Kim, J.-H. and Chun, H.-Y.: Statistics and Possible Sources of Aviation Turbulence over South Korea, Journal of Applied Meteorology and Climatology, 50, 311–324, https://doi.org/10.1175/2010jamc2492.1, 2011.

Kim, J.-H., Sharman, R., Strahan, M., Scheck, J. W., Bartholomew, C., Cheung, J. C. H., Buchanan, P., and Gait, N.: Improvements in Nonconvective Aviation Turbulence Prediction for the World Area Forecast System, Bulletin of the American Meteorological Society, 99, 2295–2311, https://doi.org/10.1175/bams-d-17-0117.1, 2018.

Kim, Y., Eckermann, S. D., and Chun, H.: An overview of the past, present and future of gravity-wave drag parametrization for numerical climate and weather prediction models, Atmosphere-Ocean, 41, 65–98, https://doi.org/10.3137/ao.410105, 2003.

Knox, J. A.: Possible Mechanisms of Clear-Air Turbulence in Strongly Anticyclonic Flows, Monthly Weather Review, 125, 1251–1259, https://doi.org/10.1175/1520-0493(1997)125<1251:pmocat>2.0.co;2, 1997.

Koch, S. E., Jamison, B. D., Lu, C., Smith, T. L., Tollerud, E. I., Girz, C., Wang, N., Lane, T. P., Shapiro, M. A., Parrish, D. D., and Cooper, O. R.: Turbulence and Gravity Waves within an Upper-Level Front, Journal of the Atmospheric Sciences, 62, 3885–3908, https://doi.org/10.1175/jas3574.1, 2005.

Krautstrunk, M. and Giez, A.: The Transition From FALCON to HALO Era Airborne Atmospheric Research, p. 609–624, Springer Berlin Heidelberg, ISBN 9783642301834, https://doi.org/10.1007/978-3-642-30183-4_37, 2012.

Kruse, C. G. and Smith, R. B.: Gravity Wave Diagnostics and Characteristics in Mesoscale Fields, Journal of the Atmospheric Sciences, 72, 4372–4392, https://doi.org/10.1175/jas-d-15-0079.1, 2015.

Kruse, C. G., Alexander, M. J., Hoffmann, L., van Niekerk, A., Polichtchouk, I., Bacmeister, J. T., Holt, L., Plougonven, R., Šácha, P., Wright, C., Sato, K., Shibuya, R., Gisinger, S., Ern, M., Meyer, C. I., and Stein, O.: Observed and Modeled Mountain Waves from the Surface to the Mesosphere near the Drake Passage, Journal of the Atmospheric Sciences, 79, 909–932, https://doi.org/10.1175/jas-d-21-0252.1, 2022.

Kunkel, D., Hoor, P., and Wirth, V.: Can inertia-gravity waves persistently alter the tropopause inversion layer?, Geophysical Research Letters, 41, 7822–7829, https://doi.org/10.1002/2014GL061970, 2014.

Kunkel, D., Hoor, P., and Wirth, V.: The tropopause inversion layer in baroclinic life-cycle experiments: The role of diabatic processes, Atmospheric Chemistry and Physics, 16, 541–560, https://doi.org/10.5194/acp-16-541-2016, 2016.

Kunkel, D., Hoor, P., Kaluza, T., Ungermann, J., Kluschat, B., Giez, A., Lachnitt, H. C., Kaufmann, M., and Riese, M.: Evidence of small-scale quasi-isentropic mixing in ridges of extratropical baroclinic waves, Atmospheric Chemistry and Physics, 19, 12 607–12 630, https://doi.org/10.5194/acp-19-12607-2019, 2019.

Lachnitt, H. C.: Consistent meteorological (ERA5) and chemical (CLaMS) information across airborne measurements over the globe between 1997 and 2023, Zenodo [data set], https://doi.org/10.5281/ZENODO.15076520, (last access: 08 September 2025), 2025.

Lachnitt, H. C., Hoor, P., Kunkel, D., Bramberger, M., Dörnbrack, A., Müller, S., Reutter, P., Giez, A., Kaluza, T., and Rapp, M.: Gravity-wave-induced cross-isentropic mixing: A DEEPWAVE case study, Atmospheric Chemistry and Physics, 23, 355–373, https://doi.org/10.5194/acp-23-355-2023, 2023.

Lane, T. P. and Sharman, R. D.: Gravity wave breaking, secondary wave generation, and mixing above deep convection in a three-dimensional cloud model, Geophysical Research Letters, 33, https://doi.org/10.1029/2006gl027988, 2006.

Lane, T. P., Reeder, M. J., and Clark, T. L.: Numerical Modeling of Gravity Wave Generation by Deep Tropical Convection, Journal of the Atmospheric Sciences, 58, 1249–1274, https://doi.org/10.1175/1520-0469(2001)058<1249:nmogwg>2.0.co;2, 2001.

Lane, T. P., Doyle, J. D., Plougonven, R., Shapiro, M. A., and Sharman, R. D.: Observations and Numerical Simulations of Inertia–Gravity Waves and Shearing Instabilities in the Vicinity of a Jet Stream, Journal of the Atmospheric Sciences, 61, 2692–2706, https://doi.org/10.1175/jas3305.1, 2004.

Lee, D.-B., Chun, H.-Y., and Kim, J.-H.: Evaluation of Multimodel-Based Ensemble Forecasts for Clear-Air Turbulence, Weather and Forecasting, 35, 507–521, https://doi.org/10.1175/waf-d-19-0155.1, 2019.

Lee, J. H., Kim, J., Sharman, R. D., Kim, J., and Son, S.: Climatology of Clear-Air Turbulence in Upper Troposphere and Lower Stratosphere in the Northern Hemisphere Using ERA5 Reanalysis Data, Journal of Geophysical Research: Atmospheres, 128, https://doi.org/10.1029/2022jd037679, 2022.

Lehmann, C. I., Kim, Y.-H., Preusse, P., Chun, H.-Y., Ern, M., and Kim, S.-Y.: Consistency between Fourier transform and small-volume few-wave decomposition for spectral and spatial variability of gravity waves above a typhoon, Atmospheric Measurement Techniques, 5, 1637–1651, https://doi.org/10.5194/amt-5-1637-2012, 2012.

Lott, F. and Miller, M. J.: A new subgrid-scale orographic drag parametrization: Its formulation and testing, Quarterly Journal of the Royal Meteorological Society, 123, 101–127, https://doi.org/10.1002/qj.49712353704, 1997.

Müller, S., Hoor, P., Berkes, F., Bozem, H., Klingebiel, M., Reutter, P., Smit, H. G. J., Wendisch, M., Spichtinger, P., and Borrmann, S.: In situ detection of stratosphere-troposphere exchange of cirrus particles in the midlatitudes, Geophysical Research Letters, 42, 949–955, https://doi.org/10.1002/2014gl062556, 2015.

Olsen, M. A., Douglass, A. R., and Kaplan, T. B.: Variability of extratropical ozone stratosphere–troposphere exchange using microwave limb sounder observations, Journal of Geophysical Research: Atmospheres, 118, 1090–1099, https://doi.org/10.1029/2012jd018465, 2013.

Orr, A., Bechtold, P., Scinocca, J., Ern, M., and Janiskova, M.: Improved middle atmosphere climate and forecasts in the ECMWF model through a non-orographic gravity wave drag parametrization, ECMWF, https://doi.org/10.21957/DM64CMPJ, 2010.

O'sullivan, D. and Dunkerton, T. J.: Generation of Inertia–Gravity Waves in a Simulated Life Cycle of Baroclinic Instability, Journal of Atmospheric Sciences, 52, 3695 – 3716, https://doi.org/10.1175/1520-0469(1995)052<3695:GOIWIA>2.0.CO;2, 1995.

Pan, L. L., Randel, W. J., Gary, B. L., Mahoney, M. J., and Hintsa, E. J.: Definitions and sharpness of the extratropical tropopause: A trace gas perspective, Journal of Geophysical Research: Atmospheres, 109, https://doi.org/10.1029/2004jd004982, 2004.

Pan, L. L., Konopka, P., and Browell, E. V.: Observations and model simulations of mixing near the extratropical tropopause, Journal of Geophysical Research Atmospheres, 111, 1–15, https://doi.org/10.1029/2005JD006480, 2006.

Plougonven, R. and Snyder, C.: Gravity waves excited by jets: Propagation versus generation, Geophysical Research Letters, 32, https://doi.org/10.1029/2005gl023730, 2005.

Plougonven, R. and Zhang, F.: Internal gravity waves from atmospheric jets and fronts, Reviews of Geophysics, 52, 33–76, https://doi.org/10.1002/2012rg000419, 2014.

Plougonven, R., Teitelbaum, H., and Zeitlin, V.: Inertia gravity wave generation by the tropospheric midlatitude jet as given by the Fronts and Atlantic Storm-Track Experiment radio soundings, Journal of Geophysical Research: Atmospheres, 108, https://doi.org/10.1029/2003jd003535, 2003.

Plougonven, R., Hertzog, A., and Teitelbaum, H.: Observations and simulations of a large-amplitude mountain wave breaking over the Antarctic Peninsula, Journal of Geophysical Research Atmospheres, 113, 1–17, https://doi.org/10.1029/2007JD009739, 2008.

Plougonven, R., Hertzog, A., and Alexander, M. J.: Case studies of nonorographic gravity waves over the Southern Ocean emphasize the role of moisture, Journal of Geophysical Research: Atmospheres, 120, 1278–1299, https://doi.org/10.1002/2014jd022332, 2015.

Plougonven, R., Jewtoukoff, V., Cámara, A. d. l., Lott, F., and Hertzog, A.: On the Relation between Gravity Waves and Wind Speed in the Lower Stratosphere over the Southern Ocean, Journal of the Atmospheric Sciences, 74, 1075–1093, https://doi.org/10.1175/jas-d-16-0096.1, 2017.

Polichtchouk, I., van Niekerk, A., and Wedi, N.: Resolved Gravity Waves in the Extratropical Stratosphere: Effect of Horizontal Resolution Increase from O(10) to O(1) km, Journal of the Atmospheric Sciences, 80, 473–486, https://doi.org/10.1175/jas-d-22-0138.1, 2023.

Rapp, M., Kaifler, B., Dörnbrack, A., Gisinger, S., Mixa, T., Reichert, R., Kaifler, N., Knobloch, S., Eckert, R., Wildmann, N., Giez, A., Krasauskas, L., Preusse, P., Geldenhuys, M., Riese, M., Woiwode, W., Friedl-Vallon, F., Sinnhuber, B.-M., Torre, A. d. l., Alexander, P., Hormaechea, J. L., Janches, D., Garhammer, M., Chau, J. L., Conte, J. F., Hoor, P., and Engel, A.: SOUTHTRAC-GW: An Airborne Field Campaign to Explore Gravity Wave Dynamics at the World's Strongest Hotspot, Bulletin of the American Meteorological Society, 102, E871–E893, https://doi.org/10.1175/bams-d-20-0034.1, 2021.

Raschendorfer, M.: The new turbulence parameterization of LM, COSMO Newsletter No. 1, pp. 89–97, 2001.

Riese, M., Ploeger, F., Rap, A., Vogel, B., Konopka, P., Dameris, M., and Forster, P.: Impact of uncertainties in atmospheric mixing on simulated UTLS composition and related radiative effects, Journal of Geophysical Research: Atmospheres, 117, https://doi.org/10.1029/2012jd017751, 2012.

Schwenk, C. and Miltenberger, A.: The role of ascent timescales for warm conveyor belt (WCB) moisture transport into the upper troposphere and lower stratosphere (UTLS), Atmospheric Chemistry and Physics, 24, 14 073–14 099, https://doi.org/10.5194/acp-24-14073-2024, 2024.

Schwenk, C. and Miltenberger, A.: The role of ascent timescales for warm conveyor belt (WCB) moisture transport into the upper troposphere and lower stratosphere (UTLS), Zenodo [data set], https://doi.org/10.5281/ZENODO.14924689, (last access: 08 September 2025), 2025.

Seifert, A.: On the parameterization of evaporation of raindrops as simulated by a one-dimensional rainshaft model, Journal of the Atmospheric Sciences, 65, 3608–3619, https://doi.org/10.1175/2008JAS2586.1, 2008.

Shapiro, M. A.: Further Evidence of the Mesoscale and Turbulent Structure of Upper Level Jet Stream–Frontal Zone Systems, Monthly Weather Review, 106, 1100–1111, https://doi.org/10.1175/1520-0493(1978)106<1100:feotma>2.0.co;2, 1978.

Shapiro, M. A.: Turbulent Mixing within Tropopause Folds as a Mechanism for the Exchange of Chemical Constituents between the Stratosphere and Troposphere, Journal of the Atmospheric Sciences, 37, 994–1004, https://doi.org/10.1175/1520-0469(1980)037<0994:tmwtfa>2.0.co;2, 1980.

Sharman, R., Tebaldi, C., Wiener, G., and Wolff, J.: An Integrated Approach to Mid- and Upper-Level Turbulence Forecasting, Weather and Forecasting, 21, 268–287, https://doi.org/10.1175/waf924.1, 2006.

Sharman, R. D. and Pearson, J. M.: Prediction of Energy Dissipation Rates for Aviation Turbulence. Part I: Forecasting Nonconvective Turbulence, Journal of Applied Meteorology and Climatology, 56, 317–337, https://doi.org/10.1175/jamc-d-16-0205.1, 2017.

Sharman, R. D., Trier, S. B., Lane, T. P., and Doyle, J. D.: Sources and dynamics of turbulence in the upper troposphere and lower stratosphere: A review, Geophysical Research Letters, 39, 1–9, https://doi.org/10.1029/2012GL051996, 2012.

Sharman, R. D., Cornman, L. B., Meymaris, G., Pearson, J., and Farrar, T.: Description and Derived Climatologies of Automated In Situ Eddy-Dissipation-Rate Reports of Atmospheric Turbulence, Journal of Applied Meteorology and Climatology, 53, 1416–1432, https://doi.org/10.1175/jamc-d-13-0329.1, 2014.

Spreitzer, E., Attinger, R., Boettcher, M., Forbes, R., Wernli, H., and Joos, H.: Modification of potential vorticity near the tropopause by nonconservative processes in the ECMWF model, Journal of the Atmospheric Sciences, 76, 1709–1726, https://doi.org/10.1175/JAS-D-18-0295.1, 2019.

Stephan, C. C., Strube, C., Klocke, D., Ern, M., Hoffmann, L., Preusse, P., and Schmidt, H.: Intercomparison of Gravity Waves in Global Convection-Permitting Models, Journal of the Atmospheric Sciences, 76, 2739–2759, https://doi.org/10.1175/jas-d-19-0040.1, 2019a.

Stephan, C. C., Strube, C., Klocke, D., Ern, M., Hoffmann, L., Preusse, P., and Schmidt, H.: Gravity Waves in Global High-Resolution Simulations With Explicit and Parameterized Convection, Journal of Geophysical Research: Atmospheres, 124, 4446–4459, https://doi.org/10.1029/2018jd030073, 2019b.

Strube, C., Ern, M., Preusse, P., and Riese, M.: Removing spurious inertial instability signals from gravity wave temperature perturbations using spectral filtering methods, Atmospheric Measurement Techniques, 13, 4927–4945, https://doi.org/10.5194/amt-13-4927-2020, 2020.

Thompson, C. F. and Schultz, D. M.: The Release of Inertial Instability Near an Idealized Zonal Jet, Geophysical Research Letters, 48, https://doi.org/10.1029/2021gl092649, 2021.

Toghraei, I., Lott, F., Köhler, L., Stephan, C. C., and Alexander, M. J.: Can Parameterizations Reproduce the Gravity Wave Momentum Fluxes and Drag Simulated by a Global High-Resolution Model?, Geophysical Research Letters, 52, https://doi.org/10.1029/2025gl115499, 2025.

Trier, S. B., Sharman, R. D., MuñOz-Esparza, D., and Lane, T. P.: Environment and mechanisms of severe turbulence in a midlatitude cyclone, Journal of the Atmospheric Sciences, 77, 3869–3889, https://doi.org/10.1175/JAS-D-20-0095.1, 2020.

Umbarkar, M.: Data used for paper "Evidence of gravity wave contribution to vertical shear and mixing in the lower stratosphere: a WISE case study", Zenodo [data set], https://doi.org/10.5281/ZENODO.17227439, 2025.

Umbarkar, M. and Kunkel, D.: Contribution of gravity waves to shear in the extratropical lowermost stratosphere: insights from idealized baroclinic life cycle experiments, Atmospheric Chemistry and Physics, 25, 10 159–10 182, https://doi.org/10.5194/acp-25-10159-2025, 2025.

Wang, M. and Fu, Q.: Stratosphere-Troposphere Exchange of Air Masses and Ozone Concentrations Based on Reanalyses and Observations, Journal of Geophysical Research: Atmospheres, 126, https://doi.org/10.1029/2021jd035159, 2021.

Wang, S. and Zhang, F.: Sensitivity of Mesoscale Gravity Waves to the Baroclinicity of Jet-Front Systems, Monthly Weather Review, 135, 670–688, https://doi.org/10.1175/mwr3314.1, 2007.

Wei, J. and Zhang, F.: Mesoscale gravity waves in moist baroclinic jet-front systems, Journal of the Atmospheric Sciences, 71, 929–952, https://doi.org/10.1175/JAS-D-13-0171.1, 2014.

Wei, J., Zhang, F., and Richter, J. H.: An Analysis of Gravity Wave Spectral Characteristics in Moist Baroclinic Jet–Front Systems, Journal of the Atmospheric Sciences, 73, 3133–3155, https://doi.org/10.1175/jas-d-15-0316.1, 2016.

Wei, J., Zhang, F., Richter, J. H., Alexander, M. J., and Sun, Y. Q.: Global Distributions of Tropospheric and Stratospheric Gravity Wave Momentum Fluxes Resolved by the 9-km ECMWF Experiments, Journal of the Atmospheric Sciences, 79, 2621–2644, https://doi.org/10.1175/jas-d-21-0173.1, 2022.

Weyland, F., Hoor, P., Kunkel, D., Birner, T., Plöger, F., and Turhal, K.: Long-term changes in the thermodynamic structure of the lowermost stratosphere inferred from reanalysis data, Atmospheric Chemistry and Physics, 25, 1227–1252, https://doi.org/10.5194/acp-25-1227-2025, 2025.

Whiteway, J. A., Pavelin, E. G., Busen, R., Hacker, J., and Vosper, S.: Airborne measurements of gravity wave breaking at the tropopause, Geophysical Research Letters, 30, 2–6, https://doi.org/10.1029/2003GL018207, 2003.

Whiteway, J. A., Klaassen, G. P., Bradshaw, N. G., and Hacker, J.: Transition to turbulence in shear above the tropopause, Geophysical Research Letters, 31, 2–5, https://doi.org/10.1029/2003GL018509, 2004.

Yoshida, L., Tomikawa, Y., Ejiri, M. K., Tsutsumi, M., Kohma, M., and Sato, K.: Large-Amplitude Inertia Gravity Waves Over Syowa Station: Comparison of PANSY Radar and ERA5 Reanalysis Data, Journal of Geophysical Research: Atmospheres, 129, https://doi.org/10.1029/2023jd040490, 2024.

Zängl, G., Reinert, D., Rípodas, P., and Baldauf, M.: The <scp>ICON</scp> (ICOsahedral Non-hydrostatic) modelling framework of <scp>DWD</scp> and <scp>MPI-M</scp>: Description of the non-hydrostatic dynamical core, Quarterly Journal of the Royal Meteorological Society, 141, 563–579, https://doi.org/10.1002/qj.2378, 2014.

Zhang, F., Davis, C. A., Kaplan, M. L., and Koch, S. E.: Wavelet analysis and the governing dynamics of a large-amplitude mesoscale gravity-wave event along the East Coast of the United States, Quarterly Journal of the Royal Meteorological Society, 127, 2209–2245, https://doi.org/10.1002/qj.49712757702, 2001.

Zhang, F., Wei, J., Zhang, M., Bowman, K. P., Pan, L. L., Atlas, E., and Wofsy, S. C.: Aircraft measurements of gravity waves in the upper troposphere and lower stratosphere during the START08 field experiment, Atmospheric Chemistry and Physics, 15, 7667–7684, https://doi.org/10.5194/acp-15-7667-2015, 2015a.

Zhang, W., Peng, J., Zhang, W., Wang, S., Li, Z., and Hanyan, W.: Sensitivity of Gravity Wave Momentum Flux Estimates on Separation Methods, Monthly Weather Review, 153, 1721–1742, https://doi.org/10.1175/mwr-d-24-0272.1, 2025.

Zhang, Y., Zhang, S., Huang, C., Huang, K., Gong, Y., and Gan, Q.: The interaction between the tropopause inversion layer and the inertial gravity wave activities revealed by radiosonde observations at a midlatitude station, Journal of Geophysical Research: Atmospheres, 120, 8099–8111, https://doi.org/10.1002/2015jd023115, 2015b.

Zhang, Y., Zhang, S., Huang, C., Huang, K., and Gong, Y.: The Tropopause Inversion Layer Interaction With the Inertial Gravity Wave Activities and Its Latitudinal Variability, Journal of Geophysical Research: Atmospheres, 124, 7512–7522, https://doi.org/10.1029/2019JD030309, 2019.

Zülicke, C. and Peters, D.: Simulation of inertia-gravity waves in a poleward-breaking Rossby wave, Journal of the Atmospheric Sciences, 63, 3253–3276, https://doi.org/10.1175/JAS3805.1, 2006.